MSc Biomedical Engineering
Assignment Report

Targeting inflammatory macrophages using bioactive liposomes to ameliorate MASLD - an in vivo biodistribution study in MASLD mouse model

Marco Bosi - s3050955

Supervisors: Prof. Dr. R. Bansal, Dr. V. Tuli
External Supervisor: Dr. Ir. JMJ Paulusse

January 31st, 2025

Department of Bioengineering Technologies
Faculty of Science and Technology
Biomedical Engineering
University of Twente

UNIVERSITY OF TWENTE.

Contents

Abstract

Metabolic dysfunction-associated steatotic liver disease (MASLD), previously called non-alcoholic fatty liver disease (NAFLD), is a prevalent metabolic condition with limited targeted treatment options. As a conclusive step in a broader project, this study explored the use of bioactive liposomes to deliver anti-inflammatory agents directly to the liver and evaluated their biodistribution and uptake in a MASLD mouse model. Cell uptake was investigated within kupffer cells, monocytes-derived macrophages and lipid-associated macrophages. Among the four liposome formulations tested, all showed significant liver accumulation, with disputable preferential uptake. Limitations such as variability in cellular uptake across different macrophage subsets and the short-term nature of the study warrant further research to optimize liposomal design and improve methodology. These findings highlight liposomes as a promising but evolving tool for MASLD management.

Keywords: MASLD, liver, liposome, cellular uptake, biodistribution, macrophages.

Chapter 1

Introduction

1.1   Liver structure and function

The liver is among the largest organs in the body. It accounts for various critical physiological processes, including metabolism, detoxification and immunity. Repeating hexagonal functional units, called lobules, constitute the hepatic tissue (Figure 1.1). Each unit is connected to the hepatic vein by central veins that allow deoxigenated blood to flow to the heart. On the other hand, the portal vein carries nutrient-rich blood from the spleen, intestines and stomach to the liver lobules [21]. The portal vein is closely grouped in a portal triad that involves a liver artery, which delivers oxygenated blood, and a bile duct. Therefore, the hepatic blood flows from this portal triad and drains to the central vein through the liver sinusoids, the radial duct of the lobule [21]. This vessel conformation allows the liver to filter approximately 30% of the total blood volume in the body each minute. As such, the organ is able to immunologically screen the blood for systemic and gut-derived pathogens. This critical role is facilitated by a diverse and specialized cellular population.

While following the liver sinusoid organization (bottom panel of Figure 1.1), the first cellular layer is shaped by the Liver sinusoidal endothelial cells (LSECs) which comprise 50% of the nonparenchymal cells of the liver. They separate the underlying hepatocytes from the blood flowing in the sinusoidal lumen. However, there is no clear boundary with the sinusoids as LSECs create a fenestrated endothelium [30]. Between the latter and the hepatocyte layer, the space of Disse (empty space visible in the very bottom of Figure 1.1, above the inferior hepatocyte monolayer) receives the plasma filtered by the overlying 100nm pores [63]. While exhibiting distinct phenotypic characteristics from vascular endothelial cells, LSECs are commonly identified as CD146+CD45- or CD31+CD45- expressing cells [25].

Furthermore, hepatocytes comprise 80% of all liver cells. These parenchymal cells play a primary role in metabolism, protein production and toxin neutralization. Nevertheless, hepatocytes can recognize pathogens and aid the host immune response [30].

They can be in direct cell-to-cell contact with Kupffer Cells (KCs), resident and non-migrating macrophages localized in the sinusoidal lumen together with neutrophils, B and T lymphocytes, and natural killer (NK) cells (Figure 1.1)[47].

Secondly, in the space of Disse Hepatic stellate cells (HSCs) are also located. In their quiescent state, HSCs are the primary storage site for vitamin A and its derivatives, playing a crucial role in retinoid metabolism. Beyond storage, they contribute to the maintenance of the extracellular matrix and support the structural integrity of the liver. Upon liver injury,
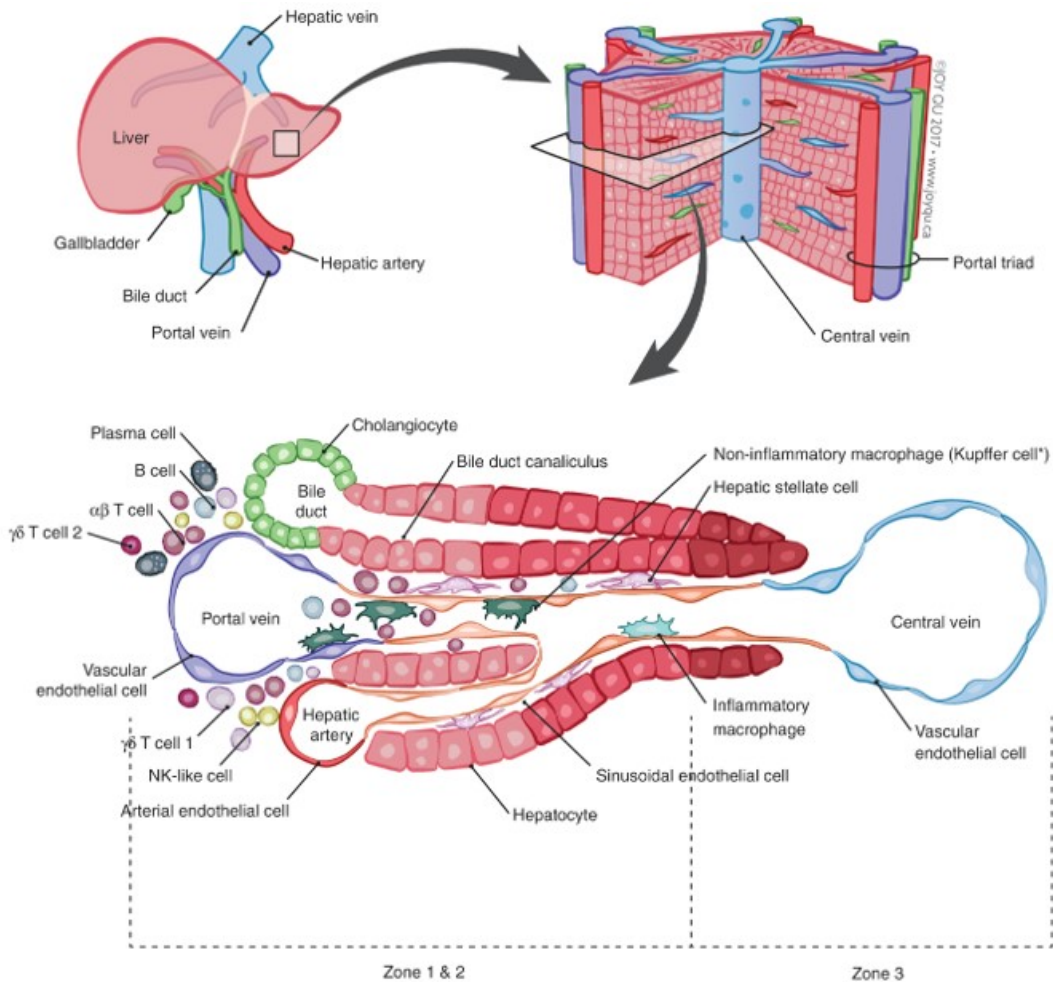
FIGURE 1.1: A cross section of a liver lobule is shown in the bottom. The figure focuses on a radial portion of the lobule while depicting the cell populations. Additional cell details are included but not pertinent to the focus of this figure. Picture adapted from [38].

HSCs become activated, switching into myofibroblast-like cells that produce extracellular matrix components, a process central to liver fibrosis [31].

1.2 MASLD pathophysiology

Metabolic dysfunction-associated steatotic liver disease or MASLD has been estimated to impact 30% of the global adult population, with its prevalence increasing from 22% to 37% from 1991 to 2019. This growth shows a concurrent trend with increasing rates of obesity and type 2 diabetes mellitus [52]. MASLD is the most common cause of chronic liver disease. As depicted in Figure 1.2, it covers a wide range of liver damage that includes MASH, advanced fibrosis, cirrhosis and liver failure [12]. MASLD previously addressed as non-alcoholic fatty liver disease (NAFLD), is the primary cause of liver-related morbidity and mortality worldwide [8].

Being a metabolic syndrome related to unhealthy lifestyle, either elevated body mass index and visceral obesity are established risk factors for MASLD. The comorbities include type-2-diabetes, hyperlipidaemia and insulin resistance.

The onset of MASLD arises from several factors, including an increased influx of free fatty acids (FFAs) from insulin-resistant adipose tissue (AT), altered hepatic metabolism of dietary lipids transported by lipoproteins, enhanced hepatic de novo lipogenesis, and impaired lipid secretion from hepatocytes [11].
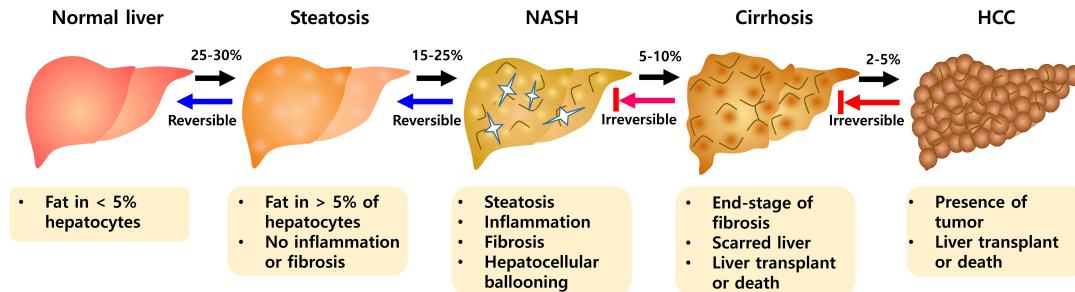

FIGURE 1.2: Schematic view of the progression of MASLD pathogenesis. The reported prevalence percentages are relative to each previous stage. NASH is the former term for MASH. Picture adapted from [47].

Metabolic dysfunction-associated steatohepatitis (MASH) is the most severe form of MASLD. Histologically, it features lobular inflammation and hepatocyte ballooning, and is correlated with a greater risk of fibrosis progression. Multiple publications show a 30% MASH prevalence among MASLD patients, in about 30-40% of MASH patients a degeneration to fibrosis and cirrhosis (Figure 1.2). From the latter patient subset, 5% develops end-stage liver disease including Hepatocellular carcinoma (HCC) [8].

Lipotoxicity   Lipid accumulation triggers a cascade of detrimental effects, termed lipotoxicity, which drives inflammation and advances MASLD toward MASH.
FFAs are physiologically metabolized into triglycerides (TGs) by de novo lipogenesis in the hepatocytes [52]. Insulin resistance impairs the suppression of lipolysis in AT, leading to elevated levels of circulating non-esterified acids or FFAs. Once taken up by the liver, FFAs are esterified into neutral TGs. However, an excess of saturated FFAs surpasses the liver's esterification capacity, triggering lipotoxicity [26]. Moreover, hepatic free cholesterol interacts with YAP-TAZ, a transcriptional regulator involved in cell proliferation and cellular reprogramming, and its expression was likewise elevated in steatotic liver tissue. Through its interaction with YAP-TAZ, free cholesterol amplified its lipotoxic effects, independent of microbial signals [52].

Disease progression   The steatosis causes a cellular stress response derived by increased protein translation, high turnover of lipid metabolism [36]. Secondly, different lipid species are recognized by extra- or intracellular pattern-recognition receptors (PRRs) which induce pro-inflammatory cytokine synthesis within hepatocytes and immune cells. Multiple cytokines play a role in driving the progression of steatohepatitis in humans, among many TNFα, IL-1 family, IL-6 or IL-11 are deemed relevant [3]. Subsequently, TNFα and chemokine (C–C motif) ligand 2 (CCL2) prompt the migration of innate immune cells including monocytes and neutrophilic granulocytes into the liver [24]. Recruited monocytes release significant levels of pro-inflammatory cytokines, driving the progression from hepatic steatosis to fibrosis [34].

1.3 Role of macrophages in MASH

Macrophages play a pivotal role in the development and progression of MASH. They are central in initiating and sustaining hepatic inflammation, a key factor in MASH pathogenesis [28].

In the liver, macrophages are categorized into two primary subsets. The first subset consists of Kupffer cells (KCs), mainly derived from yolk sac erythromyeloid progenitor cells. KCs are self-renewing, locally proliferating, and exhibit phagocytic activity. In physiological conditions, they primarily support immune homeostasis in the liver. The second subset are monocyte-derived liver macrophages (MoMFs), whose progenitors are bone marrow hematopoietic stem cells. MoMFs are recruited to the sites of inflammation and can be differentiated to secrete inflammatory mediators, upon influence of the surrounding microenvironment [53]. Moreover, macrophages are divided into two phenotypic profiles: pro-inflammatory and anti-inflammatory macrophages. The first subset produces inflammatory cytokines (IL-1, TNF-α, and IL-6), whereas the other phenotype contributes to tissue remodeling, mitigation of the inflammation and immunomodulation [27].

1.3.1 Kupffer cells

KCs are the resident and stationary macrophages. In direct contact with LSECs, they are located in the vasculature facet of the hepatic sinusoid [30]. Duffield et al. demonstrated that KCs play distinct and potentially opposing roles at different stages of liver fibrosis [13]. During the injury phase, KCs primarily promote matrix deposition and activate HSCs. In contrast, during recovery, they contribute to fibrosis resolution by increasing the production of matrix metalloproteinases (MMPs). This suggests that activated macrophages may adopt diverse phenotypes depending on the stage of liver disease. Upon steatosis and liver injury, they contribute to triggering both innate and adaptive responses [1]. Activated KCs have pro-inflammatory behavior, thus leading to hepatic oxidative stress and inflammation. Furthermore, TIM4 (T-cell immunoglobulin and mucin domain containing 4) is used to identify KCs in the liver [44].

1.3.2 Monocyte-derived macrophages

A quick decline in KCs is seen in models of diet-induced MASH and HCC [10]. It is suggested that KCs might self-renew through proliferation, although this needs further study [55]. Monocyte-derived macrophages (MoMFs) are reputed to play a key role in replenishing the macrophage population [6].

Upon liver injury, MoMFs recruitment is mainly induced by increased CCL2 secretion caused by toll-like receptor (TLR) signaling in KCs or HSCs [3]. Infiltrated monocytes produce and secrete extensive amount of pro-inflammatory cytokines, thereby promoting transition of steatosis to fibrosis [34]. In addition, infiltrated macrophages are characterized by high CD11b expression and low to intermediate F4/80 levels, whereas KCs are identified by high F4/80 expression [62].

1.3.3 Lipid-associated macrophages

Lipid-associated macrophages (LAMs) feature high lysosomal activity elevated presence of lipid-containing structures [7]. Interestingly, LAMs were similarly identified by a largely overlapping gene signature in the visceral AT of obese patients, within atherosclerotic lesions, and in livers affected by MASH [49]. Moreover, surface proteins TREM2 and GP-NMB are among the most reliable markers for identifying LAMs across tissues, with the

added benefit of being robust mRNA expression indicators. However, using TREM2 and GPNMB as surface markers for LAMs may be problematic, as both proteins can be cleaved and released into the circulation in their soluble forms [23].
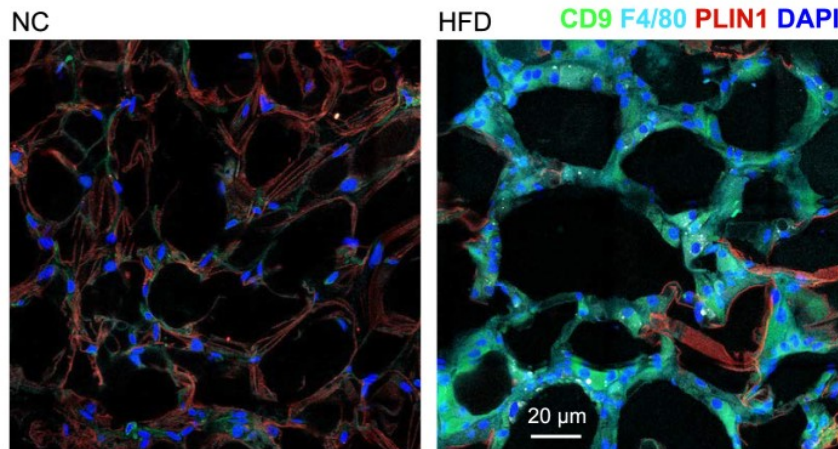

FIGURE 1.3: LAMs were identified by F4/80 (cyan), CD9 (green) markers in AT sections. Perilipin-1 (red) labels lipid droplets. On the left, 16-week-old WT mice (NC). On the right, after 12 weeks of HFD. Picture adapted from [29].

Furthermore, in diet-induced obese mice, the number of LAMs in AT depots rises with increasing adiposity, highlighting their association with metabolic state of the proximal tissue. Upon 12-week high fat diet (HFD), a considerable recruitment is shown in Figure 1.3. Such process suggests that LAMs play a key role in coordinating local nutrient availability. Consistently, LAMs within crown-like structures (CLSs) in adipose tissue uptake lipids via a TREM2-dependent mechanism, and their genetic program for lysosomal lipid metabolism regulation is conserved across humans and mice [29].

In MASLD, LAMs are widely recognized as a significant subset of recruited MoMFs [9]. In addition, in a model of early hepatic steatosis, Trem2-deficient MASH mice exhibited increased caspase 3 protein cleavage and elevated pro-apoptotic Bax expression in the liver [37]. This indicates that recruited LAMs play a role in clearing dying hepatocytes and mitigating liver damage during the early stages of the disease. However, multiples studies suggest that LAMs can acquire a pro-fibrotic phenotype during cirrhotic stage. They are reported as a subset of scar-associated macrophages (SAMs) in cirrhosis while supporting liver fibrosis via high Spp1 expression [16][49]. This suggests a deeper level of heterogeneity based on RNA signatures. LAMs expressing SAMs markers could be addressed in a therapeutic strategy aimed at inhibiting their pro-fibrotic activity. On the other hand, an alternative therapeutic option lies in focusing on the LAMs not expressing SAMs marker with the aim of supporting their anti-inflammatory behavior while preventing the deleterious phenotype shift.

1.4 Current treatment approaches

Current MASLD management strategies include lifestyle interventions, pharmacotherapy, and surgical options. The cornerstone of MASLD treatment involves lifestyle changes aimed at weight reduction and management of metabolic comorbidities. Implementing a Mediterranean-like dietary pattern with calorie restriction and increasing physical activity are recommended strategies [4].

While lifestyle changes are fundamental, pharmacological treatments can complement these efforts. The primary therapeutic strategies are based on: eradicating the stimulus or harmful cause, suppressing hepatic inflammation, obstructing the activation of HSCs, supporting the deterioration of extracellular matrix [2].

It is important to note that the management of MASLD should be individualized, taking into account the patient's overall health, the presence of comorbidities, and the severity of liver disease. Moreover, MASLD is a slowly progressing condition, thereby causing many challenges to short-term clinical goals [64].

Glucagon-like peptide-1 (GLP-1) is an incretin hormone that regulates appetite, glycaemic levels while being gastric emptying. Notably, GLP-1 receptor agonists have demonstrated effectiveness in reducing liver fat and improving MASH liver histology. However, no significant regression of fibrosis was observed [43].

Another pathway that have been therapeutically explored involves peroxisome proliferator-activated receptor (PPAR) is a nuclear receptor that has a considerable influence on energy handling, inflammation and fibrinogenesis [19]. In AT and quiescent HSCs, PPARγ is the primary type. Pioglitazone, a PPARγ agonist, promotes MASH resolution and reduces fibrosis severity, though not achieving full one-stage regression. Additionally, it improves glycaemic control, lipid profiles, and cardiovascular outcomes, particularly in atherosclerotic CVD [39].

Resmetirom (Rezdiffra), an oral, liver-targeted thyroid hormone receptor- selective drug showed positive results after completing a Phase 3 trial. The latter resulted in MASH resolution and fibrosis improvement. This trial was designed to assess drug safety and efficacy, the related results are thought to predict further clinical benefits [22]. Recently, it has been conditionally approved by FDA to be used together with diet and exercise for non-cirrhotic MASH adults [32].

1.4.1 Therapeutic targeting

Hepatic macrophages are compelling therapeutic targets because of their critical role in maintaining liver homeostasis, acting as first responders to liver damage, and exhibiting both pro-disease and anti-disease functions in liver conditions. In this current project, the focus is kept on targeting macrophages. The primary approaches in targeting these immune cells can be summarized to: hinder inflammatory cell recruitment (monocytes and macrophages), inhibit macrophage activation, modulate macrophage function and polarization [59].

As discussed in Paragraph 1.3.2, MoMFs are recruited in the injured liver via chemoattractant cytokines such as CCL2 and CRR2/5 [54]. A CCR2/CCR5 antagonist, cenicriviroc, interferes with these two pro-inflammatory pathways by inhibiting them. It gained positive histological results in MASH patients [20].

1.4.2 Liposomal drug delivery

Liposomes are one of the most widely used drug delivery system to deliver both hydrophilic and hydrophobic drugs [45]. Liposomes are biodegradable and biocompatible vesicles with a phospholipid membrane and aqueous core. They are readily phagocytosed by macrophages, particularly KCs, leading to liver accumulation [51]. However, cationic liposomes may induce cytokine activation and cellular membrane disruption [14]. Liposomes designed for hepatic macrophage targeting are typically around 100nm in size, suitable for passive targeting strategies.

Liposomes are effective carriers for delivering anti-inflammatory agents such as dexamethasone, curcumin, and calcitriol to the liver, showing superior outcomes compared to free drugs in mouse models of acute and chronic liver diseases [5]. Pharmacokinetic studies reveal that liposomes primarily accumulate in the liver, targeting not only KCs but also monocytes, infiltrating macrophages, and, to a lesser degree, T cells. Additionally, they potentially promote macrophage repolarization to a regulatory phenotype [40].

1.4.3   Previous work

Former master's students in the PDT group designed various liposomal formulations aimed at targeting liver macrophages to reduce inflammation and mitigate consequent liver fibrosis. This section provides a concise overview of the drugs delivered and the underlying rationale for the different strategies employed to target hepatic macrophages.

N-3 long-chain polyunsaturated fatty acids (n-3 LCPUFAs), particularly docosahexaenoic acid (DHA), are known for their positive effects on lipid metabolism, cardiovascular health, and inflammation key factors. DHA supplementation has shown superior therapeutic potential compared to other n-3 LCPUFAs, due to its ability to produce maresin 1 (MaR1). MaR1, a macrophage pro-resolving mediator, promotes anti-inflammatory macrophage polarization via the MaR1-ROR-12-LOX pathway, reducing inflammation and improving tissue homeostasis.
Utilizing DHA, a stable precursor metabolized into MaR1 by macrophages, presents a viable alternative. Liposomes can enhance DHA local anti-inflammatory effect by delivering it directly to the liver, where it accumulates due to the organ reticuloendothelial system (RES) activity. Moreover, cholesterol sulfate (CS), a natural ROR agonist, can further amplify this effect by facilitating anti-inflammatory polarization.
Kampen et al. proposes a liposomal delivery system co-encapsulating DHA and CS to synergistically target liver inflammation. The approach leverages the MaR1-ROR-12-LOX circuit to reduce immune cell migration, F4/80 expression, and overall inflammation, offering a promising strategy for managing MASLD progression [60].

Pro-inflammatory macrophages rely on aerobic glycolysis, while anti-inflammatory macrophages primarily utilize oxidative phosphorylation [61]. Itaconate, a metabolite derived from the TCA cycle, exhibits anti-inflammatory, anti-oxidative, and anti-bacterial properties, making it a promising therapeutic agent. Itaconate exerts its effects by inhibiting succinate dehydrogenase (SDH), activating Nrf2, and modifying key glycolytic enzymes, thereby reducing reactive oxygen species, suppressing pro-inflammatory cytokines like IL-1 and IL-6, and shifting macrophages towards an anti-inflammatory phenotype.
However, native itaconate cannot permeate cells. Its derivative, 4-octyl itaconate (4-OI), offers enhanced cell permeability but suffers from low bioavailability. Liposomal delivery systems provide a solution by enabling targeted delivery of 4-OI to the liver, a reticuloendothelial system (RES)-rich organ where macrophages uptake the liposomes [60].

Besides targeting the intracellular pathways involved in inflammatory macrophages, different cell surface markers, expressed on activated macrophages, were explored to deliver anti-inflammatory drug (e.g. Prednisolone) with the final aim of inhibiting macrophage-driven inflammation. The strategy additionally included deploying competitive compounds to occupy the membrane-bound receptor and inhibit pro-inflammatory signaling cascades triggered by its activation.

Mincle, also known as Clec4e, is a type II transmembrane receptor. It plays a key role as a pattern recognition receptor by identifying pathogen-associated molecular patterns (PAMPs) and damage-associated molecular patterns (DAMPs). Its carbohydrate recognition domain binds PAMPs, while a separate domain recognizes DAMPs. Signal transduction occurs via the Fc receptor γ-chain (FcRγ), leading to activation of spleen tyrosine kinase (Syk) and the NF-κB pathway.

This results in pro-inflammatory cytokine production (e.g. IL-1, IL-6) and stimulation of Th1 and Th17 immune responses, driving the recruitment of immune cells such as MoMFs and neutrophils.

Mincle recognizes mycobacterial trehalose-6,6'-dimycolate and its synthetic analogs, with affinity increasing for ligands with longer fatty acid chains. The optimal compound is a trehalose lipid derivative (T6-P) [56].

FcγR1 (CD64) is a high-affinity receptor for IgG, playing a key role in immune responses, including phagocytosis, antigen presentation, and cytokine secretion. It uniquely binds monomeric and polymeric IgGs through its three Ig-like extracellular domains. FcγR1 expression is induced by IFNα, IFNγ, and IL-12 and is predominantly found on pro-inflammatory CD14+ macrophages, monocytes, neutrophils, eosinophils, and dendritic cells. However, its expression varies across macrophage subsets. FcγR1 activates pro-inflammatory downstream signaling pathways, leading to immune activation [56].

Chapter 2

Aim and objectives

To examine the in vivo and cellular distribution of liposomal formulations in MASLD mouse model.

To address the aim of the project, the following objectives were established:

(i) To prepare labelled liposomes;

(ii) To characterize the liposome formulations;

(iii) To study the organ biodistribution and liver uptake of the liposomal formulations in vivo;

(iv) To examine the cell distribution and cellular uptake of the liposomal formulations via flow cytometer and immunohistochemical stainings.

2.1   Hypotheses

The following hypotheses were formulated to guide the investigation:

- Preferential uptake of the liposomal formulations by the liver;

- Higher uptake by macrophages;

- Differential uptake of different liposomal formulations by different macrophage populations.

Chapter 3

Materials and methods

3.1 Materials

1,2-dipalmitoyl-sn-glycerol-3-phosphocholine (DPPC) (Avanti Lipids), docosahexaenoic acid (DHA) (Cayman Chemical Company), cholesterol sulfate (CS) (Sigma-Aldrich), 4-octyl itaconate (4-OI) (abcr), 1,2 dihexadecanoyl-sn-glycero-3-phospho-(1'-rac-glycerol) sodium salt (DPPG) (Sigma-Aldrich), trehalose lipid derivative (T6-P) (Sigma-Aldrich Chemie GmbH), 1,2-distearoyl-sn-glycerol-3-phosphoethanolamine (DSPE mPEG) (Cayman Chemical Company), 1,2-distearoyl-sn-glycero-3-phosphoethanolamine-N- -[dibenzocyclooctyl(polyethylene glycol)2000] ammonium salt (DSPE-PEG-DBCO) (Avanti Lipids), Cholesterol (Sigma-Aldrich), PEG-2000-C-DMG (Avanti Lipids), 1,1'-Dioctadecyl-3,3,3',3'-Tetramethylindotricarbocyanine Iodide (DiR) (MedChemExpress), 1-palmitoyl-2-(dipyrrometheneboron difluoride)undecanoyl-sn-glycero-3-phosphocholine (Topfluor PC) (Avanti Lipids), DSPE PEG-Cy7 (Avanti Lipids).

Some of the other chemicals used were: phosphate buffered saline (PBS) (Sigma-Aldrich), ethanol (EtOH) (Supelco), methanol (Sigma-Aldrich), isopropanol (Sigma-Aldrich), potassium chloride (KCl) (Sigma), sodium chloride (NaCl) (Merck), Carbon tetrachloride (CCl_4) (Sigma-Aldrich), Olive oil (Sigma-Aldrich).

Some of the employed tools were: tissue homogenizer gentleMACS (Miltenyi Biotec), Zetasizer (Malvern instruments), Lipofast LF-50 extruder (Avastin), plate reader Infinite 200 PRO (Tecan Ltd).

3.2 Formulations of liposomes

There were four different treatments of interest as explained in Section 1.4.3. The formulations employed in this project had minor variations from those produced in the efficacy studies. The main reasons derived from the use of different fluorescent labels, tailored for the desired analysis. As suggested by Figure 3.1, all the formulations were synthesized via hot ethanol injection with few process modifications that are elucidated in the following paragraphs.
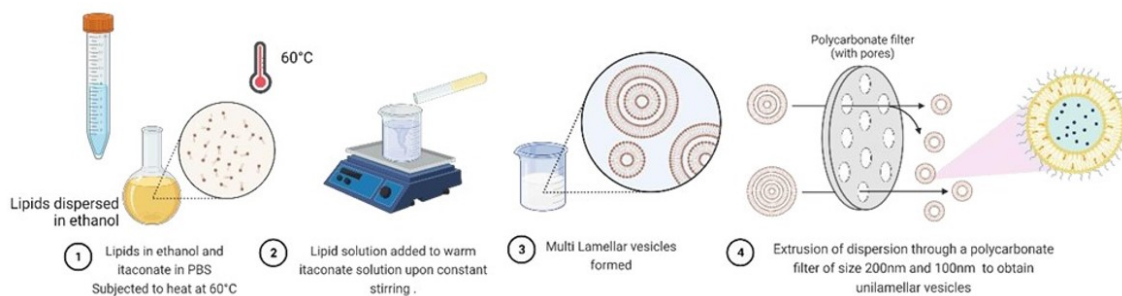
FIGURE 3.1: Schematic view of hot ethanol injection. The inserted description points at 4-OI, however the procedure was commonly employed for all liposome formulations. Figure adopted from [48].

3.2.1 DHA-CS liposomes

To produce this formulation, lipids and DHA were mixed in mol% proportions - DPPC: DHA: CS: DSPE PEG: Cy7: TopFluor PC to be 57:20:20:2:0.5:0.5. As CS does not dissolve in ethanol alone [41], the lipids were dissolved in a solution, made by 60μl of methanol and 240μl of ethanol, with a final concentration of 78,8mM/ml (Table 3.1).

DHA-CS Lip	Molecular weight	Mol% (g/mol)	mg in 0.3ml
DPPC	733.56	57.00	9.88
DHA	328.49	20.00	1.55
Cholesterol	386.65	0.00	0.00
Cholesterol sulfate Na	488.70	20.00	2.31
DSPE PEG	2803.78	2.00	1.66
DSPE PEG Cy7	3302.09	0.50	0.21
TopFluor PC	909.97	0.50	0.12

TABLE 3.1: Detailed composition of DHA-CS Liposomes.

In the meantime, 5ml of PBS was pre-heated to 60°C. The pre-heated PBS was magnetically stirred and the ethanol solution containing the lipids was added to it in a continuous stream. The solution was left to stir for 5-7 minutes, so the liposomes could self-assemble. Next, the solution was poured in the Lipofast LF-50 extruder, connected to the pre-heated PBS. The suspension was extruded as follows: 5 times extrusion upon 200 nm polycarbonate membrane (Sartorius) and afterward 5 times extrusion upon 100 nm polycarbonate membrane (Whatman).
The liposomes were then dialyzed at 4°C against PBS using a dialysis tubing cellulose membrane (Sigma-Aldrich Chemie GmbH) with 14 kDa cut off for 24 hours on a magnetic stirrer at 100 rpm.

In the control liposome, cholesterol replaced Cholesterol Sulfate. In this case, lipids and DHA were mixed in mol% proportions - DPPC: DHA: Cholesterol: DSPE PEG: TopFluor to be 57:20:20:2:0.5:0.5. The lipids were dissolved in 0.3ml of pure ethanol with a final concentration of 78,80mM/ml. The next synthesis steps are the same ones mentioned for the DHA-CS formulation. Detailed composition of control liposomes is included in the Appendix (Table 7.1).

3.2.2 4-OI liposomes

To produce this formulation, lipids were mixed in mol% proportions - 4-OI: DPPC: DSPE PEG: Cy7: TopFluor PC to be 60:37:2:0.5:0.5. The lipids were dissolved in 0,4ml of pure ethanol with a final concentration of 50,5mM/ml (Table 3.2).

4-OI Lip	Molecular weight (g/mol)	Mol%	mg in 0.4ml
4-OI	242.31	60.00	3.17
DPPC	733.56	37.00	6.00
Cholesterol	488.70	0.00	0.00
DSPE PEG	3077.80	2.00	1.22
DSPE PEG Cy7	3302.09	0.50	0.28
TopFluor PC	909.97	0.50	0.16

TABLE 3.2: 4-OI liposome composition.

The following extrusion and dialysis process are the same described in the DHA-CS liposome preparation (Paragraph 3.2.1).

In the control liposome, cholesterol replaced 4-OI. In this case, lipids were mixed in mol% proportions - DPPC: Cholesterol : DSPE PEG: Cy7: TopFluor PC to be 65:32:2:0.5:0.5. The next synthesis steps are the same ones mentioned for the 4-OI formulation. Detailed composition of control liposomes is included in the Appenidx (Table 7.2).

3.2.3 T6P liposomes

To produce this formulation, lipids were mixed in mol% proportions - DPPC: DPPG: Cholesterol: T6P: DiR: TopFluor PC to be 28.5:3:40:28:0.5:0.5. The lipids were dissolved in 0,5ml of pure ethanol with a final concentration of 161.08mM/ml (Table 3.3). The compound T6P is indeed a T6-P derivative named Trehalose 6-hexadecanoate.

T6P Lip	Molecular weight (g/mol)	Mol%	mg in 0.5ml
DPPC	733.56	28.50	16.84
DPPG	744.95	3.00	1.80
Cholesterol	386.65	40.00	12.46
T6P	580.71	28.00	13.10
DiR	1013.40	0.50	0.40
TopFluor PC	909.97	0.50	0.41

TABLE 3.3: T6P liposome composition.

The following extrusion and dialysis process are the same described in the DHA-CS liposome preparation (3.2.1).

In the control liposome, an increased DPPC amount replaced T6P. In this case, lipids were mixed in mol% proportions - DPPC: DPPG: Cholesterol: DiR: TopFluor PC to be 56.5:3:40:0.5:0.5. The lipids were dissolved in 0,5ml of pure ethanol with a final concentration of 161.08mM/ml. The next synthesis steps are the same ones mentioned for the 4-OI formulation. Detailed composition of control liposomes is included in the Appenidx (Table 7.3).

3.2.4 FcGR1 liposomes

To produce this formulation, lipids were mixed in mol% proportions - DPPC: Cholesterol: FcGR1: DSPE PEG DBCO: DiR: TopFluor PC to be 57:40:1.92:2.5:1.0:0.5. The lipids were dissolved in 0,5ml of pure ethanol with a final concentration of 77.59mM/ml (Table 3.4).

FcGR1 Lip	Molecular weight (g/mol)	Mol%	mg in 0.5ml
DPPC	733.56	57.00	16.22
Cholesterol	386.65	40.00	6.00
FcGR1 azide	1989.09	1.92	0.75
scrambled FcGR1 azide	1989.09	0.00	0.00
DSPE PEG DBCO	3077.80	2.50	2.99
DiR	1013.40	1.00	0.40
TopFluor PC	909.97	0.50	0.20

TABLE 3.4: FcGR1 liposome composition

The following extrusion is the same as in the DHA-CS liposome preparation (Paragraph 3.2.1). Next, FcγR1-azide was dissolved in DMSO with a 20mg/ml concentration, it was then conjugated to the extruded liposomes. The active compound FcGR1 is in reality a FcγR1-targeting derivative created from (6-Azido)-KLRSQECDWEEISVK called also FcγR1-azide (ChinaPeptides Co., Ltd.).

In the control liposome, scrambled FcGR1 (sFcGR1 or (6-Azido)-DWCEIEVQKSRKLES) replaced FcGR1. In this case, lipids were mixed in mol% proportions - DPPC: Cholesterol: sFcGR1: DSPE PEG DBCO: DiR: TopFluor PC to be 57:40:1.92:2.5:1.0:0.5. The lipids were dissolved in 0,5ml of pure ethanol with a final concentration of 77.59mM/ml. The same conjugation process of the treatment formualtion was adopted. Detailed composition of control liposomes is included in the Appenidx (Table 7.4).

3.3 Characterization of liposomes

3.3.1 Size and ζ potential

The size, the polydispersity index (PDI) were measured by using dynamic light scattering (DLS) and the zeta potential was analyzed via surface charge quantification using Malvern Zetasizer. From the liposome formulation, 5 μl were diluted in 1 ml of PBS for DLS measurement. Whereas, 5 μl were diluted in 1 ml of 10mM KCl for zeta potential measurement.

3.3.2 Fluorescent stain concentration

Two different dyes were included in each liposome formulation. One for the in vivo imager (PEARL) and one for the flow cytometer (BD FACSAria II). The former was DSPE PEG-Cy7 (756/779nm) for DHA-CS, 4-OI liposomes and respective controls. Instead, DiR (748/780nm) was in the formulations of T6-P, FcγR1 liposomes and relative controls. On the other hand, Topfluor PC was employed for liposome labelling in FACS in every formulation.

Fluorescence signals from 10 μl of each sample were measured while using the in vivo imager. Whereas, in order to record Topfluor PC fluorescence, the multimode plate reader was used. 100 μl of liposome sample was placed in 96-well flat bottom black plate and the fluorescent spectrum was obtained.

3.4   CCl$_4$-induced liver inflammation mouse model

40 mice were ordered to conduct the biodistribution study. 8 weeks old male C57BL/6J mice from Janvier Labs were housed in the animal facility of the University of Twente over the 6 weeks duration of the study. 20 animals for the treatments and 20 for the respective control formulations. By doing so, 8 different mice group were created, in which 5 mice were randomly placed (Table 3.5).

Group	Pre-treatment (IP)	IV treatment	Treatment volume (μl)
DHA-CS	CCl$_4$ (0,2ml/kg)	DHA-CS Cy7-liposome	100
4-OI	CCl$_4$ (0,2ml/kg)	4-OI Cy7-liposome	100
T6P	CCl$_4$ (0,2ml/kg)	T6-P DiR-liposome	100
FcGR1	CCl$_4$ (0,2ml/kg)	FcγR1 DiR-liposome	150

TABLE 3.5: Treatment groups for in vivo biodistribution study. IV treatment column refers to intravenous injection of the different liposome formulations. Control groups are being ignored for clarity sake.

Mice were fed with western diet and high glucose/fructose water with weekly dosing of CCl4 for 5 weeks. The latter was performed with a progressive CCl$_4$ dose, from 0.05ml/kg to 0.2ml/kg, while accounting for a mouse average body weight of 20g [58]. Once a week, the animals received an intraperitoneal injection of 100μl (solvent: olive oil) of CCl$_4$, in order to induce acute liver injury. Specifically, on day 1, 8, 15, 22 and 29.
The day after the fifth pre-treatment admnistration (Day 30 in Figure 3.2), the mice were injected intravenously with the different liposome treatments as described in the last column of Table 3.5.
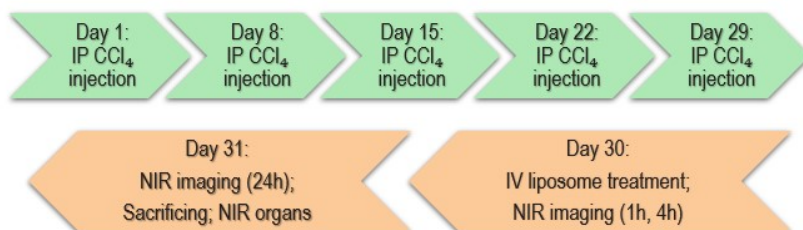

FIGURE 3.2: View of the animal study timeline with focus on the pre-treatement and the final imaging steps. NIR stands for near infra-red.

The mice were anesthetized with isoflurane and imaged at 1h, 4h, and 24h following liposome administration using the PEARL Trilogy in vivo imager, configured to acquire signal from the 700nm channel for both DiR and Cy7-labelled liposomes.

After 24 hours, the mice were euthanized by cervical dislocation, and major organs-including the liver, kidneys, spleen, lungs, and heart-were harvested, placed as shown in Figure 3.3, imaged using the same device. Signal quantification was performed with Image Studio software (version 5.2.5, LI-COR Biosciences).
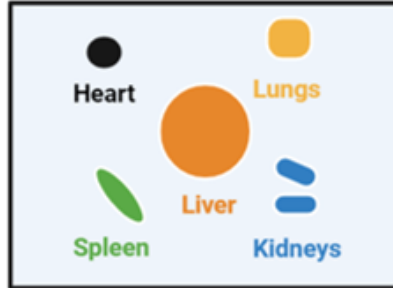

FIGURE 3.3: Schematic view of organ placement. All the organs were placed following this pattern before the organ distribution analysis.

3.5 Cell isolation from mouse livers

With the help of twizzers and scalpel, excised livers were cut into small pieces and suspended in DMEM with L-glutamine (0% FBS). The liver tissue fragments were placed into gentleMACS C tubes, which were then filled with dissociation media (DMEM with L-glutamine (0% FBS) with 1mg/ml Collagenase A, 10U/ml DNase I) to overflow and sealed while inverted.

The tubes were later positioned at RT in the gentleMACS Dissociator and homogenized by following 37_m_LIDK_1 program. Next, after resuspending the samples, they were filtered through a MACS Smart Strainer (100μm).

They were then centrifuged at 300g for 10 minutes. The pellets were suspended in 1000μl of 2% FBS in PBS. After 3 washing and centrifuge (300g for 5 minutes) steps, the pellets were dissolved in new FBS/PBS solution.

From the biggest pellets, few cells were collected for the unstained control. Next, 100μl were aliquoted in Eppendorfs linked to marker based antibodies as described in Table 3.6. The vials with multiple antibodies are explained in the next paragraph 3.6.1.

Vial	Antibody	Fluorophore
Mx1	Unstained	-
Mx2	Hoechst (Invitrogen, 2291647)	DAPI
Mx3	CD11b (Biolegend, 101228)	Pe.Cy5.5
Mx4	CD45 (Biolegend, 103106)	Pe
Mx5	TREM2 (R&DSystems, FAB17291A)	AF647
Mx6	CD146 (Biolegend, 134712)	APC
Mx7	DUMP	PeDazzle594
Mx8	TIM4 (Biolegend, 130004)	AF647
Mx9	F4/80 (Biolegend, 123114)	Pe.Cy7
Mx10	All A	-
Mx11	All B	-
Mx12	All C	-

TABLE 3.6: Schematic view of antibodies added to cells collected from mice livers for in vivo biodistribution study. The last 3 rows refer to 3 different antibody mixes done for the respective panels that were analyzed.

After 45 minute incubation at 4°C, unbound probes were flushed by two washing and 500g centrifuge steps. Next, the cells were fixed by using a 4% formaldehyde in PBS for 20 minutes. Then, the samples were washed 3 times with FBS/PBS solution and spinned 3 times for 5 minutes 300g. Before running them via FACS, Hoechst was added in the vials of interest.

3.6   Flow cytometry - uptake study

The aim here is to measure the treatment absorption within the liver macrophage environment. The macrophages subpopulations that were assessed were KCs, MoMFs and LAMs. They were respectively recognized by Tim4, CD11b^{high} and F4/80^{int}, Trem2. In addition, LSECs uptake was measured by tagging their CD146 marker. The cells were analyzed with BD FACS AriaII flow cytometer and the FACS Diva software with the data acquisition set to 20,000 events.

3.6.1   Gating strategy

For three of the mentioned cell subsets, a distinctive cell panel was layed out as shown in the following tables.
Unstained samples and mono-stained samples were used together to draw the gates. As shown in Figure 3.4 placed as an example, the unstained and the Hoechst stained cells from a mouse were relevant to set the Hoechst gate. The unstained cells showed events that were negative for Hoechst, so it was possible to create a gate that excluded them. It was then validated and adjusted by overlaying the Hoechst positive population plot.
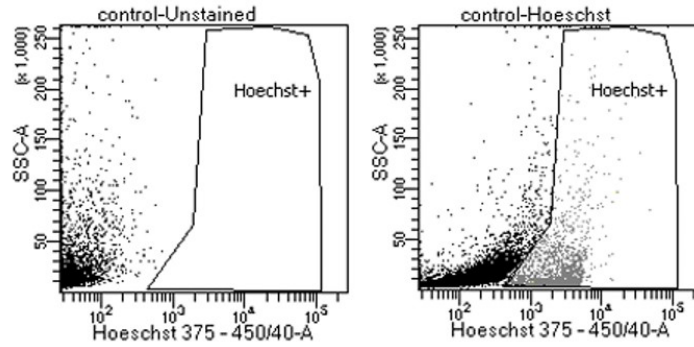
FIGURE 3.4: View of the method followed to draw Hoechst gate. On the left, unstained control and besides the single stained Hoechst sample are shown.

Nucleated cells were identified by positive Hoechst staining. Both macrophage panels involved a DUMP gate that was helpful for collecting monocytes and macrophages from Leukocytes (CD45+ cells). The DUMP gate derived from multiple antibodies. They were CD3, NK1.1, CD19 and Ly6G, used to tag T/B cells, NK cells, B cells Neutrophils and Myeloid-derived suppressor cells. These cells were disregarded from the analyzed panels, only DUMP- cells were retained by inverting the DUMP gate.

LSECs Panel

The strategy to detect how many LSECs absorbed the liposome treatments is based on the tags shown in Table 3.7. Gates were created with the method mentioned in the second paragraph of 3.6.1. In this case, nucleated cells were gated based on negative CD45 expression (non-leukocytes). Next, CD146 positive cells were selected by plotting CD45-events in CD146 vs side scatter graph.

Antibody	Fluorophore	Filter
Unstained	-	-
Hoechst	DAPI	375-450/50
CD45	Pe	488-585/42
CD146	APC	633-660/20
All A	-	-

TABLE 3.7: Flow panel for Liver sinusoid endothelial cells.

After selecting the interested cell population, liposome signal was detected and recorded in that specific population. All treatments were tagged with Topfluor PC that has emission in the FITC channel. Therefore, after gating Hoechst+, CD45-, and CD146+ events, multiple and identical liposome positive gates were set. Through this approach, data regarding liposome uptake by the targeted cell populations were systematically collected.

KCs Panel

The strategy to detect how many KCs absorbed the liposome treatments is based on the tags shown in Table 3.8. Gates were created with the method mentioned in the second paragraph of 3.6.1. Starting from the negative DUMP events, F4/80 was plotted against CD11b to distinguish two macrophage subsets. The first one, MoMFs, shows CD11b^{high} and F4/80^{int} events. Whereas, the second one, resident macrophages, exhibits CD11b^{int} and F4/80^{high} events.

While taking into account only the DUMP- cells, KCs were selected by assessing Trem2 expression.

Antibody	Fluorophore	Filter
Unstained	-	-
Hoechst	DAPI	375-450/50
CD45	Pe	488-585/42
DUMP	PeDazzle594	488-616/23
TIM4	AF647	633-660/20
F4/80	Pe.Cy7	488-780/60
CD11b	Pe.Cy5.5	488-695/40
All B	-	-

TABLE 3.8: Flow panel for Kupffer cells.

By following the same procedure mentioned in the last part of LSECs paragraph, liposome positive events were identified from most of the sorted cell populations, in order to visualize the absorbed treatment distribution within the flow panel.

LAMs Panel
The strategy to detect how many LAMs absorbed the liposome treatments is based on the tags shown in Table 3.9. Gates were created with the method mentioned in the second paragraph of 3.6.1. Common gating process was used for KCs, there are exceptions in the final steps. By considering DUMP negative cells, LAMs were identified through Tim4 positive events. Furthermore, LAMs population was displayed on CD11b vs F4/80 plot to validate their overlay with MoMFs.

Antibody	Fluorophore	Filter
Unstained	-	-
Hoechst	DAPI	375-450/50
CD45	Pe	488-585/42
DUMP	PeDazzle594	488-616/23
TREM2	AF647	633-660/20
F4/80	Pe.Cy7	488-780/60
CD11b	Pe.Cy5.5	488-695/40
All C	-	-

TABLE 3.9: Flow panel for Lipid-associated macrophages.

By following the same procedure mentioned in the last part of LSECs, liposome positive events were identified from most of the sorted cell populations, in order to visualize the absorbed treatment distribution within the flow panel.

3.7 Uptake analyses

As mentioned previously, the liposome signal (marked by FITC probe) was recorded for cell sets and subsets of interest that were sorted along the different flow panels. Among the cell groups studied, population A consists of CD45+DUMP+ cells. Whereas, B relates to CD45+DUMP- cells, namely macrophages and monocytes. The ratio of liposome positive

events of these two cell sets is relative to liposome positive leukocytes (CD45+ cells). While focusing on population B, data about liposome positive MoMFs, macrophages and LAMs was derived from LAMs flow panel. These uptake percentages are relative to population B positive to treatment. Furthermore, starting from KCs flow panel, insights on liposome positive KCs, MoMFs and macrophages were drawn.

3.8   Immunohistochemistry and immunofluorescence

Cryosections (6μm) were cut using a Leica CM 3050 cryostat (Leica Microsystems). An hydrophobic pen was used to circle the sections. Cryosections were air-dried and fixed in 10% formalin (4% formaldehyde) (Sigma-Aldrich) for 20 minutes at RT. Primary antibodies were diluted 1:100 in PBS. After three rinsing steps with non-filtered PBS, 75μl of antibody solution were added on sections that were incubated overnight at 4°C. In the next day, secondary antibodies were diluted 1:100 in 5% mice serum containing PBS. After 3 rinsing steps with non-filtered PBS, 75μl of antibody solution were added on sections which were incubated for 1 hour at RT in the dark.
Then, LipidTOX (Invitrogen) was diluted 1:500 in PBS. After 3 rinsing steps with non-filtered PBS, 75μl of solution were added before a 30 minutes incubation. Later, one drop of DAPI mounting medium (Sigma-Aldrich) was added on each section. The slides were stored at 4°C in the dark and then imaged with Nikon Ti-E inverted fluorescence microscope. Further image analysis was done via ImageJ (ImageJ2).

3.9   Statistical analyses

Data regarding organ absorption are presented as mean $\pm$ SEM. Cell uptake data are shown as mean $\pm$ SD. The graphs and statistical analyses were carried out using Graphpad Prism (9.5.1 version). Differences between groups were assessed by two-tailed unpaired student t-test. The differences were considered significant at $p < 0.05$.

Chapter 4

Results and discussion

4.1 DHA-CS liposomes

The DHA-CS liposome was synthesized following Kampen's work where it was previously assessed [60]. She performed an animal efficacy study and found promising results, derived from decreased expression of collagen I and reduced inflammation (F4/80 staining). Here, minor modifications were made on the formulation to incorporate different dyes. In Figure 4.1, the used treatment and control particles are shown. Their center is the aqueous core, the yellow lipid bilayer is made of DPPC.
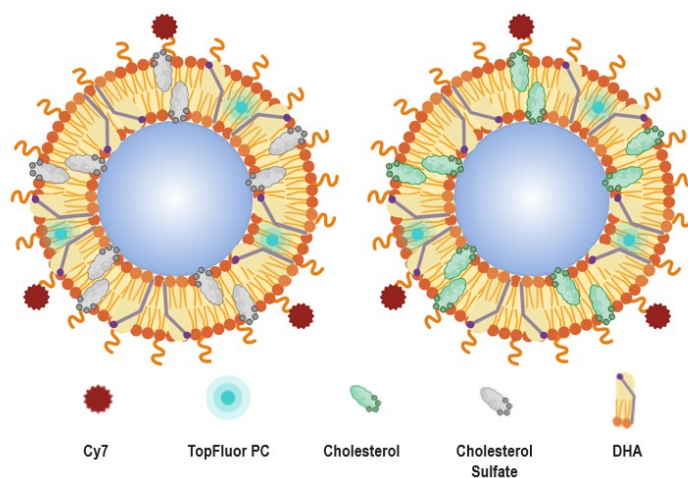
FIGURE 4.1: Model of the synthesized liposomes. On the right, the DHA-CS particle is showed with CS marked in grey, in the bilayer together with TopFluor PC in light blue and the elongated DHA molecule. On the surface, Cy7 in burgundy and PEG chains in orange are displayed. On the left side, the control liposome has cholesterol in green instead of CS.

4.1.1 Characterization of liposomes

The liposomes were characterized for diameter, PDI and zeta potential. DLS was used to analyze DHA and DHA-CS liposome (Table 4.1). The formulations were extruded through membranes that have 200 and 100nm cutoff. Both particles exceed these values, probably due to low stability and aggregation. Cholesterol has a fluidifying effect on DPPC saturated tails [50]. The reduction in size, from DHA to DHA-CS formulation, suggests that

CS has a stabilizing effect on the lipid bilayer. CS is known to increase membrane packing density and reduce fluidity [17]. It carries also a sulfate group that contributes to the more negative surface charge of DHA-CS liposome.

Liposomes	Size by number in PBS (d.nm ± SD)	Polydispersity index (PdI ± SD)	ζ potential in KCl (mV ± SD)
DHA Lip	505.0 ± 55.02	0.65 ± 0.16	-6.46 ± 0.69
DHA-CS Lip	287.9 ± 51.15	0.30 ± 0.04	-21.60 ± 2.41

TABLE 4.1: Size and zeta potential of DHA-CS and control liposomes. In the size analysis, there was one single peak in the distribution. The size derives from it. d.nm refers to the diameter expressed in nm.

4.1.2 In vivo biodistribution study

To investigate the in vivo organ distribution of DHA-CS liposome in C57BL/6J mice, Cy7 fluorescent dye was utilized for near-infrared (NIR) imaging. Mice were treated with 100 µL of DHA and DHA-CS liposomes. The signals were captured using the PEARL Trilogy whole-animal NIR imaging system.

This study employed an MASLD mouse model with C57BL/6J mice, and imaging was performed at 1 hour, 4 and 24 hours post-liposome injection. The 1-hour time point was used to assess the early distribution of the treatment, providing insights into their rapid accumulation in specific tissues, which could indicate potential safety concerns or off-target effects. The 4-hour time point allowed sufficient circulation time for the liposomes, enabling analysis of their interaction with various organs and tissues to identify patterns of accumulation, clearance, or redistribution. This time point helped determine whether the liposomes were rapidly eliminated or retained in specific tissues. The 24-hour assessment offered a longer-term perspective on particle retention, revealing whether they exhibited time-dependent accumulation in certain organs or if they were cleared from the system by this point [15].

Figure 4.2 shows on the right representative pictures of the different groups at 1h, 4h and 24h. While DHA liposome has similar localization, the treatment displays a peritoneal absorption that grows over time. It provides a higher fluorescent signal than the control with a peak at 4h. The lungs, heart, spleen, liver, and kidneys are excised because they represent key organs involved in the biodistribution, clearance, and potential off-target effects of liposomes. As the first capillary bed encountered post-IV injection, lungs may trap larger particles or aggregates. The heart reflects systemic circulation and potential cardiac exposure. Next, the spleen is part of the RES, often responsible for clearing nanoparticles from circulation. Lastly, the kidneys are involved in excretion of smaller molecules or degraded components of liposomes [57].

In Figure 4.3, the retention signal from these major organs is presented. The organs were placed by following the scheme shown in Figure 3.3. DHA-CS liposome absorption in the liver is higher than the control. The remaining organs show poor retention levels, thus suggesting a liver specific delivery after 24h post-injection. A complete biodistribution panel is reported in the Appendix (Figure 7.1).
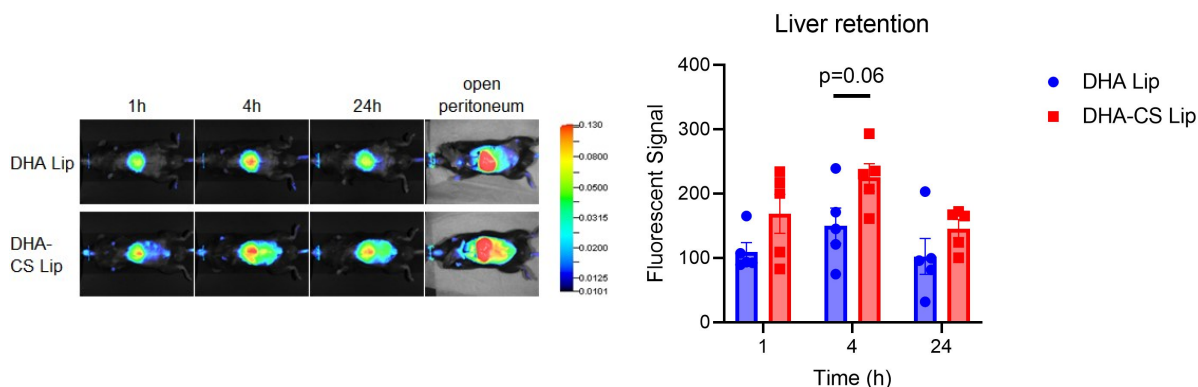
FIGURE 4.2: On the left, a representative in vivo localization images for each treatment condition at 1h, 4h and 24h time points. On the right side, a plot showing quantification of signal localized in the liver region for both liposomes at 1h, 4h and 24h time point.
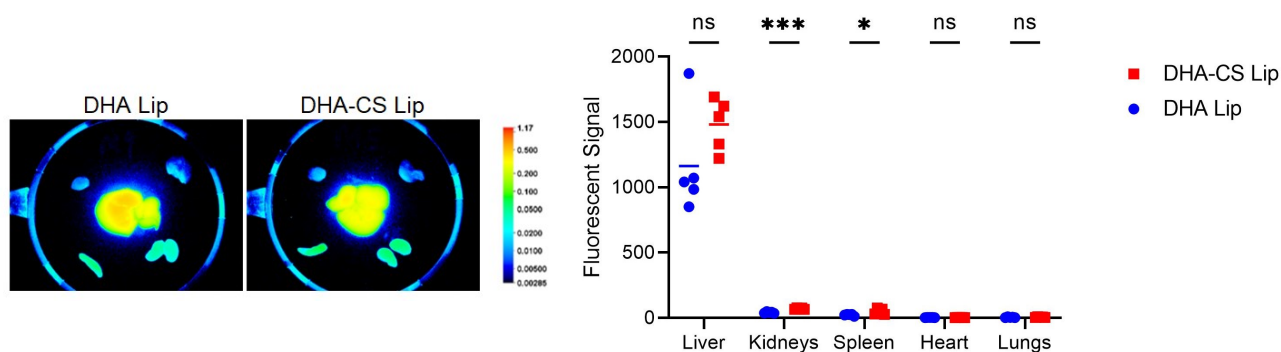

FIGURE 4.3: On the left, a representative image of fluorescent signal in excised organs from control and treatment conditions. In the center lays the liver, on the top right and then clockwise there are: lungs, kidneys, spleen and heart. On the right, it is plotted a relative localization of fluorescent signal in the excised organs.

4.1.3 FACS analysis of liver samples

The liver is an immune-rich organ, hosting a diverse range of immune cells. To investigate how the monocyte/macrophage immune cell profile varied across different treatment groups, fluorescence-assisted cell sorting (FACS) was utilized.

Small liver samples were processed according to the method described in Section 3.5, as a preparatory step for FACS analysis. As summarized in Table 3.6, multiple fluorophores were employed to label the cells, enabling the identification of distinct populations within the tissue samples.

The standard procedure for staining and calibrating the flow cytometer suggests including additional samples stained with every antibody except one. This step was omitted to streamline the extensive workflow, then only the unstained samples were used for preparing the tool and setting the gates.

Figure 4.4 shows the plots from mouse 1, treated with DHA-CS liposomes and stained with all the antibodies involved in LAMs panel.

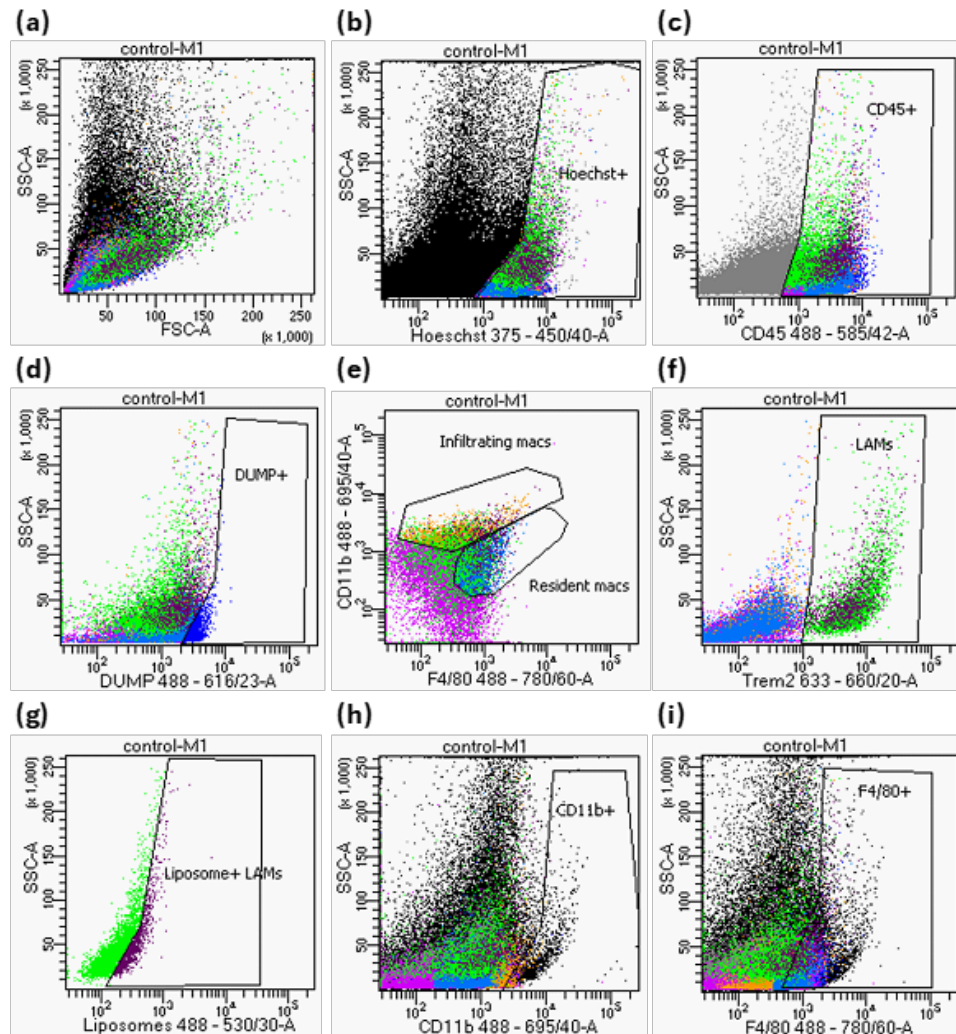The central graph (e) aimed at sorting two immune cell subsets out of DUMP- cells:

FIGURE 4.4: Populations positive for respective antigen expression plotted on fluorophore spectrum: (a) Side scatter vs forward scatter of all cells visualized; (b) Nucleus containing cells selected from total population using Hoechst; (c) Leukocytes selected from nucleated cells based on CD45 antigen expression; (d) Cells expressing Ly6G, CD3, CD19, NK1.1 antigens (DUMP+) selected from the CD45+ population and excluded from the analysis; (e) DUMP negative population selected for the expression of CD11b and F4/80 antigens; (f) DUMP- population selected for the expression of Trem2 antigen; (g) Trem2+ population selected for the expression of FITC (liposome); (h) nucleated cells sorted for CD11b expression; (i) nucleated cells selected for F4/80 antigen.

MoMFs (infiltrating macs) as CD11b^{high} and F4/80^{int} and resident macrophages (simply called macrophages) as CD11b^{int} and F4/80^{high}. The plotted events do not show two distinct populations, whereas, (f) displays a clear Trem2 positive subset (LAMs) from DUMP-events. Similarly in (g), the treatment positive events are untied from the treatment negative Trem2 + cells. Furthermore, (h) illustrates a limited CD11b positive population, likely due to suboptimal antibody binding or fluorescence quenching. This explains the reason behind the highly compact distribution reported in (e). Finally, the last 2 plots were used to support the data presented in (e) and to validate staining quality.

The gating hierarchy is presented in Figure 4.5. It shows the organization of the different cell populations that were analyzed. In addition, the extent of the liposome uptake recording can be comprehended.
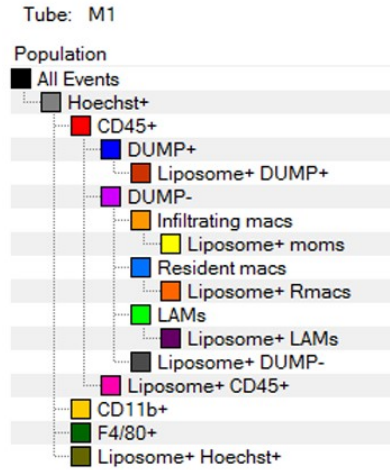

FIGURE 4.5: Gating hierarchy employed for LAMs identification for cells derived from mice liver from biodistribution study.

Secondly, a flow panel to identify KCs was employed (Figure 7.9). The procedure is very similar to LAMs panel with the exception of few steps where Tim4 antibodies were used to sort KCs out of DUMP- events ((d) and (e)). The resulting plots were not completely consistent with the common ones derived from the previous panel, then the unmatching parts were stressed in Figure 7.9 attached in the Appendix. In this case, Tim4 positive events were quite poor (d), probably for ineffective antibody binding. Similarly, CD45 positive events were unexpectedly limited (a). Furthermore, the hierarchy used in KCs panel is illustrated in Figure 7.10 in the Appendix.

Lastly, flow cytometry results for LSECs were not included in the results of this thesis, as they were deemed less relevant to the primary focus on macrophage-targeted liposomal uptake.

Differential uptake of treatment As stated in Paragraph 3.7, the liposome signal (FITC probe) was recorded for cell sets and subsets sorted across various flow panels. Population A consists of CD45+DUMP+ cells, while Population B includes CD45+DUMP- cells, representing macrophages and monocytes. The ratio of liposome-positive events for these groups was compared to liposome-positive leukocytes (CD45+ cells).
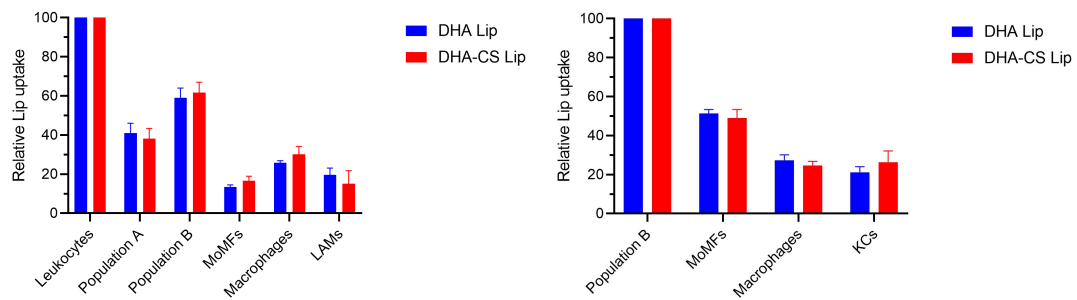
FIGURE 4.6: Percent positive populations for DHA-CS liposome uptake. On the left, focus on treatment positive LAMs. On the right, uptake from KCs.

Focusing on Population B, data for liposome-positive MoMFs, macrophages, and LAMs were obtained from the LAMs flow panel, with percentages relative to treatment-positive Population B. Additionally, liposome-positive KCs, MoMFs, and macrophages were analyzed from the KCs flow panel (4.6).

The left plot shows a higher macrophage retention and a comparative uptake from MoMFs and LAMs. From the other graph, MoMFs had more positive events, whereas KCs and macrophages have equal ones.

As debated in Paragraph 4.1.3, the panels for LAMs and KCs demonstrated distinct CD45+ populations, with the second dataset exhibiting significantly lower levels. As a result, it is not feasible to directly compare the data between KC and LAM populations. Consequently, the liposome uptake by these two cell subsets cannot be reliably compared.

4.1.4 Immunohistochemical staining

work in progress

4.2   4-OI liposomes

The 4-OI liposome was synthesized following Kampen's work where it was previously assessed [60]. She performed an animal efficacy study and found promising results, derived from decreased expression of collagen I and reduced inflammation (F4/80 staining). Here, minor modifications were made to the formulation to use different dyes. In Figure 4.7, the used treatment and control particles are shown. Their center is the aqueous core, the yellow lipid bilayer is made of DPPC.
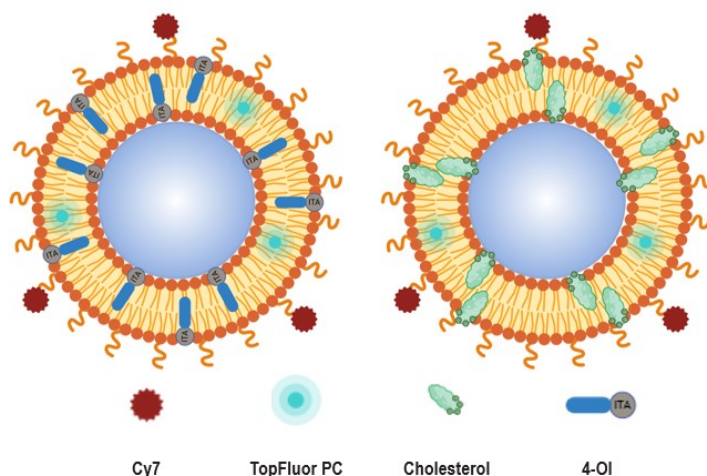

FIGURE 4.7: Model of the synthesized liposomes. On the right, the 4-OI particle is showed with 4-OI compound marked in grey and cyan, in the bilayer together with TopFluor PC in light blue. On the surface, Cy7 in burgundy and PEG chains in orange are displayed. On the left side, the control liposome has cholesterol in green instead of the itaconate derivative.

4.2.1   Characterization of liposomes

The liposomes were characterized for diameter, PDI and zeta potential. DLS was used to analyze empty and 4-OI liposome (Table 4.2). The formulations were extruded through membranes that have 200 and 100nm cutoff. Both particles greatly exceed these values, probably due to low stability and aggregation. The control size distribution is broadly polydispersed, as PdI > 0.4. It showed a single peak, the unique peak size was considered. On the other hand, the 4-OI formulation is moderately polydispersed and did not present a single-peaked distribution, thus the z-average fitting was used to obtain size data.
Regarding surface charge, zeta potential of 4-OI particles is more negative than the control. This is likely due to deprotonation of one of 4-OI carboxyl groups. This happens at physiological pH, thus the molecule contributes to the negative charge of the liposome [46].

Liposomes	Size by number in PBS (d.nm ± SD)	Polydispersity index (PdI ± SD)	ζ potential in KCl (mV ± SD)
Empty Lip	393.7 ± 66.16	0.53 ± 0.11	-2.88 ± 0.94
4-OI Lip	486.0 ± 17.6	0.19 ± 0.19	-4.28 ± 0.96

TABLE 4.2: Size and zeta potential of 4-OI and control liposomes. In the size analysis, there was one single peak in the control distribution. The size derives from it, in 4-OI the z-avg fit was used.

4.2.2 In vivo biodistribution study

To investigate the in vivo organ distribution of 4-OI liposome in C57BL/6J mice, Cy7 fluorescent dye was utilized for near-infrared (NIR) imaging. Mice were treated with 100 µL of empty and 4-OI liposomes. The signals were captured using the PEARL Trilogy whole-animal NIR imaging system.

Figure 4.8 shows on the right representative pictures of the different groups at 1h, 4h and 24h. While the empty liposome has a contained and similar localization over time, the treatment mice display a peritoneal absorption that grows over time. The latter provides a considerably higher fluorescent signal than the control with a peak at 4h. On the contrary, control samples show a lower absorption level that gradually increases with time.
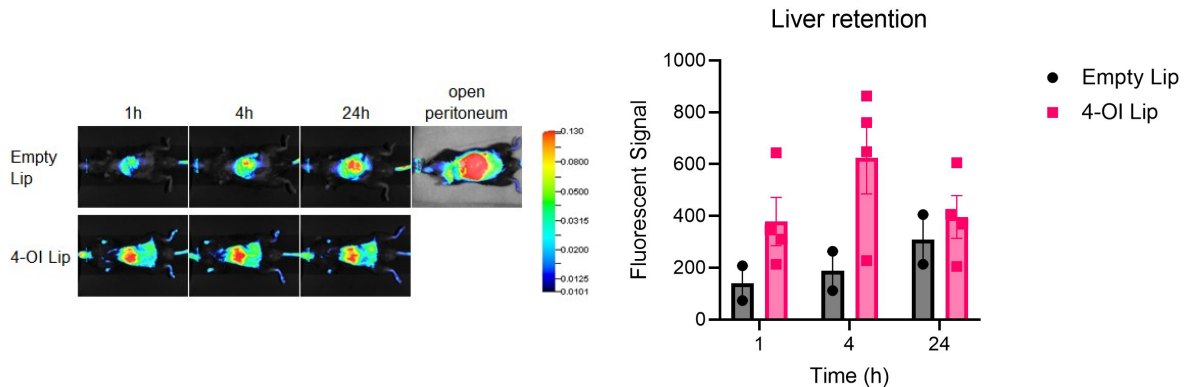

FIGURE 4.8: On the left, a representative in vivo localization images for each treatment condition at 1h, 4h and 24h time points. On the right side, a plot showing quantification of signal localized in the liver region for both liposomes at 1h, 4h and 24h time point.

In Figure 4.9, the retention signal from heart, liver, kidneys, lungs and spleen is presented. The organs were placed by following the scheme shown in Figure 3.3. Empty liposome absorption in the liver is higher than 4-OI samples. The remaining organs show poor retention levels, thus suggesting a liver specific delivery after 24h post-injection. A complete biodistribution panel is shown in the Appendix (Figure 7.3).
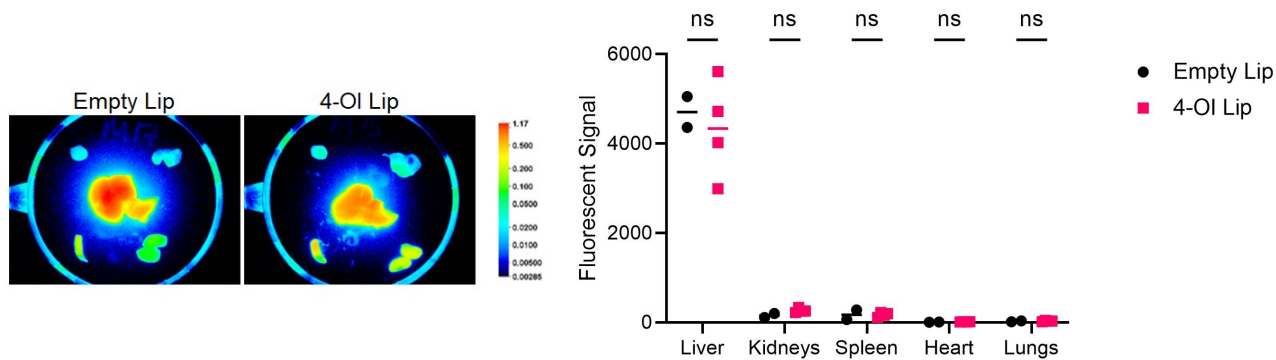
FIGURE 4.9: On the left, a representative image of fluorescent signal in excised organs from control and treatment conditions. In the center lays the liver, on the top right and then clockwise there are: lungs, kidneys, spleen and heart. On the right, it is plotted a relative localization of fluorescent signal in the excised organs.

4.2.3 FACS analysis of liver samples

The flow cytometer results for both panels were thoroughly consistent with FACS results from DHA-CS treated samples. Therefore, see Paragraph 4.1.3 and the related pictures. The material related to KCs flow panel is attached in the Appendix (Figure 7.10 and 7.9). Lastly, flow cytometry results for LSECs were not included in the results of this thesis, as they were deemed less relevant to the primary focus on macrophage-targeted liposomal uptake.

Differential uptake of treatment As stated in Paragraph 3.7, the liposome signal (FITC probe) was recorded for cell sets and subsets sorted across various flow panels. Population A consists of CD45+DUMP+ cells, while Population B includes CD45+DUMP- cells, representing macrophages and monocytes. The ratio of liposome-positive events for these groups was compared to liposome-positive leukocytes (CD45+ cells).
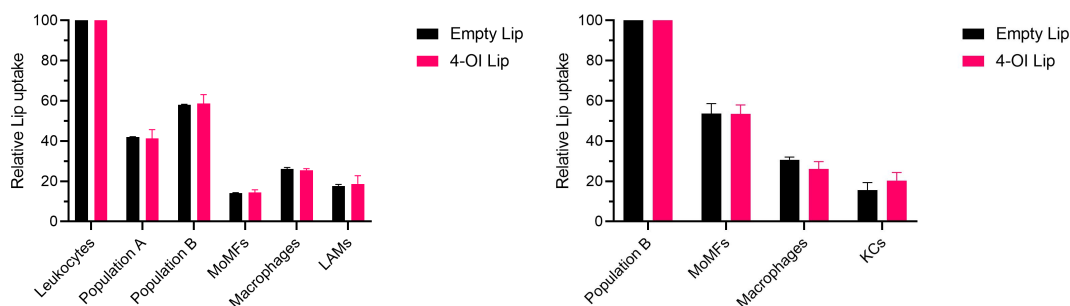

FIGURE 4.10: Percent positive populations for 4-OI liposome uptake. On the left, focus on treatment positive LAMs. On the right, uptake from KCs.

Focusing on Population B, data for liposome-positive MoMFs, macrophages, and LAMs were obtained from the LAMs flow panel, with percentages relative to treatment-positive Population B.
The left plot shows a higher macrophage retention and a comparative uptake from MoMFs and LAMs.

Additionally, liposome-positive KCs, MoMFs, and macrophages were analyzed from the KCs flow panel (Figure 4.10). MoMFs had more positive events. Macrophages show approximately 25% uptake and KCs 20%.

As debated in Paragraph 4.2.3, the panels for LAMs and KCs demonstrated distinct CD45+ populations, with the second dataset exhibiting significantly lower levels. As a result, it is not feasible to directly compare the data between KCs and LAMs populations. Consequently, the liposome uptake by these two cell subsets cannot be reliably compared. By only examining LAMs panel related to the left plot, MoMFs and LAMs exhibit similar uptake levels.

4.2.4 Immunohistochemical staining

work in progress

4.3 T6P liposomes

The T6P liposome was synthesized following Szachniewicz's work where it was previously assessed [56]. His synthesized particles had Prednisolone phosphate (PLP) as cargo, a gluco-corticoid drug. He performed an animal efficacy study and found promising results, derived from decreased expression of pro-inflammatory surface markers (CD14, FcR1) and augmented anti-inflammatory surface markers (CX3CR1, CD206). In this current project, minor modifications were made on the formulation, by neglecting the cargo and employing different dyes for the biodistribution analysis. In addition, Szachniewicz conducted encapsulation efficiency tests for T6P liposomes and performed stability assays. However, these assessments were not included in the analysis due to time constraints.

In Figure 4.11, the used treatment and control particles are shown. Their center is the aqueous core, the yellow lipid bilayer is made of DPPC.
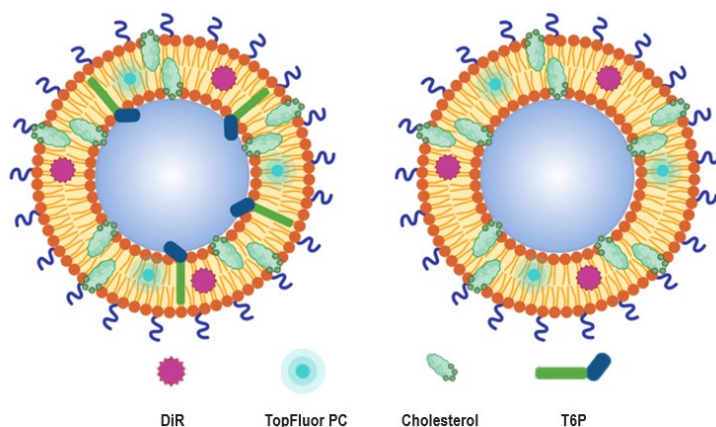

FIGURE 4.11: Model of the synthesized liposomes. On the right, the T6P particle is showed with T6P marked in green and blue, in the bilayer together with TopFluor PC in light blue and DiR in lilac. On the surface, DPPG chains are displayed in blue. On the side, the control liposome lacks the T6P derivative.

4.3.1 Characterization of liposomes

The liposomes were characterized for diameter, PDI and zeta potential. DLS was used to analyze empty and T6P liposome (Table 4.3). The formulations were extruded through membranes that have 200 and 100nm cutoff. T6P particles greatly exceeds the filter values, probably due to low stability and aggregation. While, the control formulation presents an appropriate size, as it has an average diameter of 132nm. The latter showed a monodispersed distribution and more than one peak. On the other hand, the treatment size distribution is broadly polydispersed, as PdI > 0.4.

Furthermore, it is relevant to remember that T6P refers to a T6-P derivative, namely Trehalose 6-hexadecanoate. Secondly, T6P liposomes were more negatively charged than the control ones. The reason lays likely in the free hydroxyl groups hosted in the trehalose moiety. At physiological pH these groups engage in hydrogen bonding or weak ionization, amplifying the negative charge [18].

Liposomes	Size by number in PBS (d.nm ± SD)	Polydispersity index (PdI ± SD)	ζ potential in KCl (mV ± SD)
Empty Lip	131.7 ± 2.4	0.11 ± 0.01	-4.36 ± 0.48
T6P Lip	270.2 ± 7.8	0.58 ± 0.05	-19.47 ± 2.41

TABLE 4.3: Size and zeta potential of T6P and control liposomes. In the size analysis, z-avg fit was used.

4.3.2 In vivo biodistribution study

To investigate the in vivo organ distribution of T6P liposome in C57BL/6J mice, the lipophilic DiR fluorescent dye was utilized for near-infrared (NIR) imaging. Mice were treated with 100 µL of empty and T6P liposomes. The signals were captured using the PEARL Trilogy whole-animal NIR imaging system.

Figure 4.12 shows on the right representative pictures of the different groups at 1h, 4h and 24h. Both liposomes display a contained and similar liver localization over time. The control mice exhibits a slightly increased peritoneal absorption that grows over time. The latter provides a marginally higher fluorescent signal than the treatment, while having a peak at 24h post IV injection.
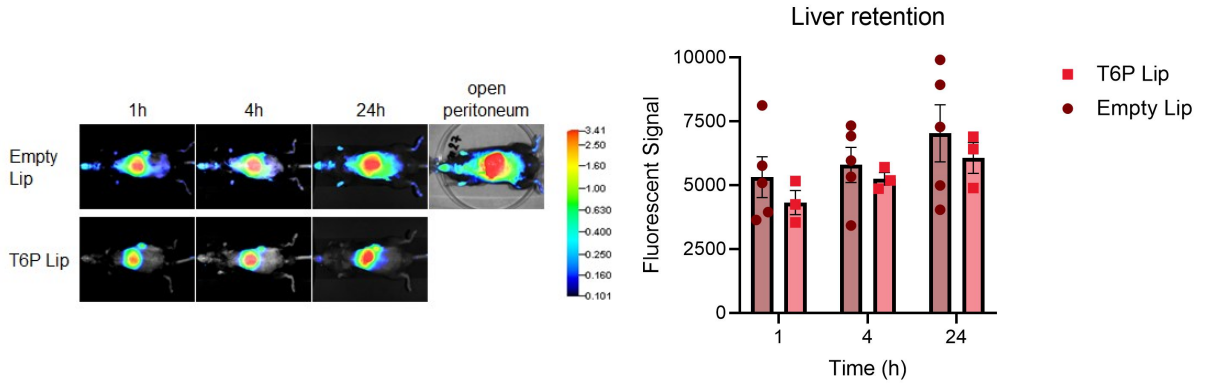

FIGURE 4.12: On the left, a representative in vivo localization images for each treatment condition at 1h, 4h and 24h time points. On the right side, a plot showing quantification of signal localized in the liver region for both liposomes at 1h, 4h and 24h time point.

In Figure 4.13, the retention signal from heart, liver, kidneys, lungs and spleen is presented. The organs were placed by following the scheme shown in Figure 3.3. Empty liposome absorption in the liver is slightly higher than T6P samples but not significantly. The remaining organs show poor retention levels, with the exception of the spleen which exhibits minor uptake in both conditions. This may be attributed to suboptimal stealth properties conferred by DPPG (compared with PEG), making the particles more recognizable to monocytes, which likely facilitated their clearance from circulation [33][35]. A complete biodistribution panel is reported in the Appendix (Figure 7.5).
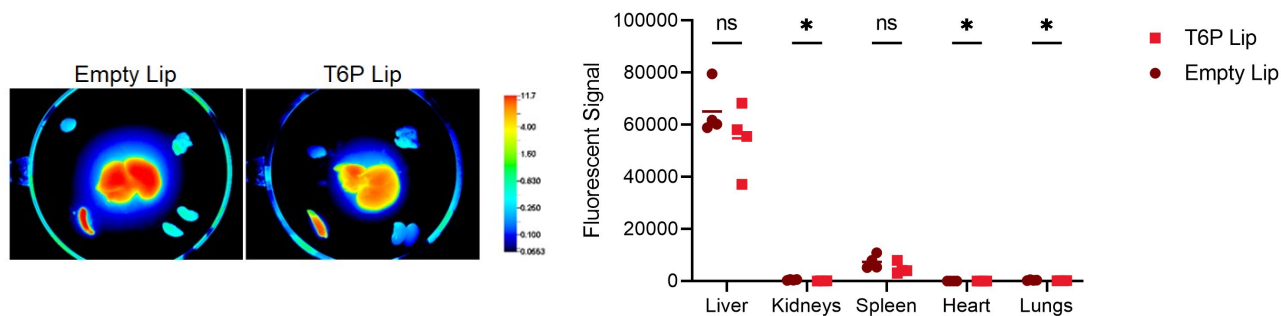
FIGURE 4.13: On the left, a representative image of fluorescent signal in excised organs from control and treatment conditions. In the center lays the liver, on the top right and then clockwise there are: lungs, kidneys, spleen and heart. On the right, it is plotted a relative localization of fluorescent signal in the excised organs.

4.3.3 FACS analysis of liver samples

See Paragraph 4.1.3, as the gating procedure was unchanged. In addition, the hierarchy scheme is available in Figure 4.5 for LAMs panel.

The samples treated with T6P liposome were organized in a new batch, different from the one containing DHA-CS and 4-OI related cells. The results deriving from this second batch present significant variations (Figure 4.14), likely due to some batch to batch disparity. In Figure 4.14, (h) shows a considerable and expected CD11b positive population among nucleated cells. Thanks to this optimal CD11b antigen binding, a good and complete distribution is found also in (e), where MoMFs and resident macrophages are two noticeable subsets. On the other hand, Trem2 positive events do not shift significantly from the other DUMP- cells.

Secondly, a flow panel to identify KCs was employed. The procedure is very similar to LAMs panel with the exception of few steps where Tim4 antibodies were used to sort KCs out of DUMP- events ((d) and (e)). The resulting plots were not completely consistent with the common ones derived from the previous panel, then the unmatching parts were stressed in Figure 7.11 attached in the Appendix. In this case, Tim4 positive events were quite poor (d), probably for ineffective antibody binding.

Similarly, CD45 positive events were unexpectedly limited (a). Consequently, DUMP-events (b) were penalized together with MoMFs and macrophages volumes (c). Furthermore, the hierarchy used in KCs panel is illustrated in Figure 7.10 in the Appendix.

Lastly, flow cytometry results for LSECs were not included in the results of this thesis, as they were deemed less relevant to the primary focus on macrophage-targeted liposomal uptake.

Differential uptake of treatment As stated in Paragraph 3.7, the liposome signal (FITC probe) was recorded for cell sets and subsets sorted across various flow panels. Population A consists of CD45+DUMP+ cells, while Population B includes CD45+DUMP-cells, representing macrophages and monocytes. The ratio of liposome-positive events for these groups was compared to liposome-positive leukocytes (CD45+ cells). Focusing on Population B, data for liposome-positive MoMFs, macrophages, and LAMs were obtained from the LAMs flow panel, with percentages relative to treatment-positive Population B. The left plot shows a higher LAMs retention and a comparative uptake from MoMFs
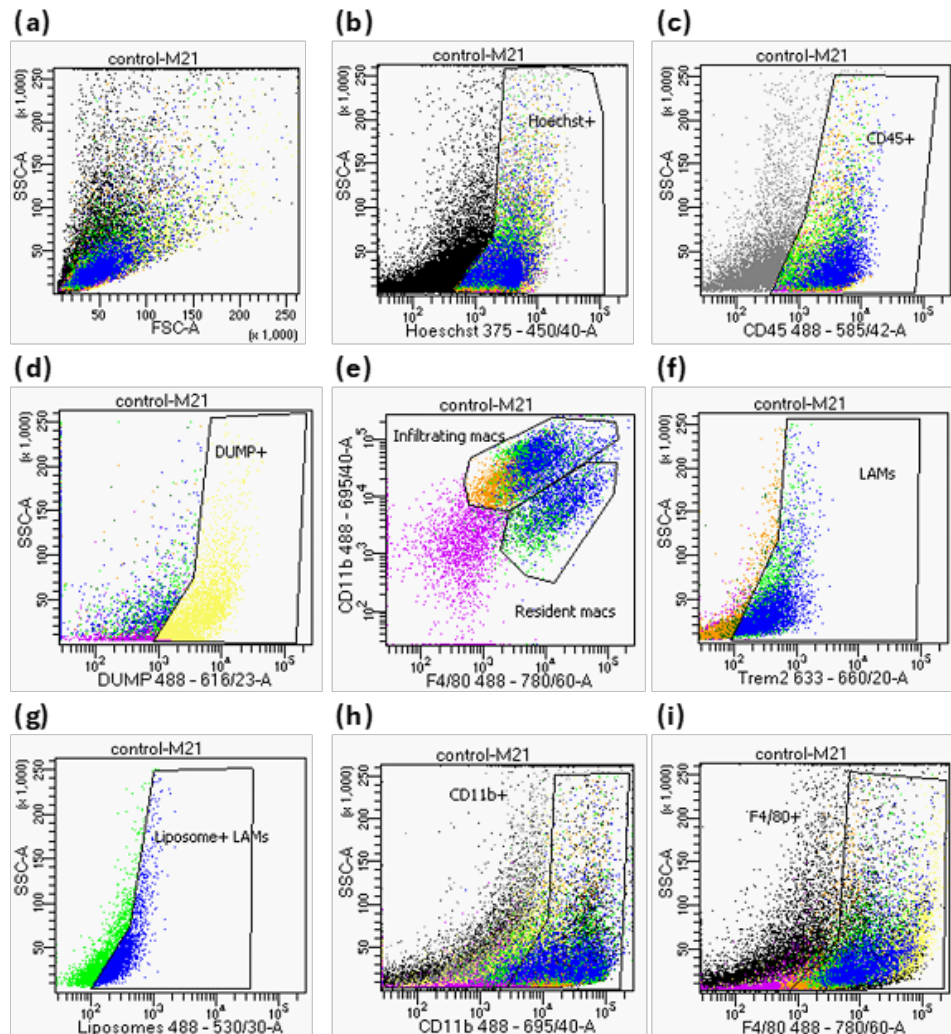
FIGURE 4.14: Populations positive for respective antigen expression plotted on fluorophore spectrum: (a) Side scatter vs forward scatter of all cells visualized; (b) Nucleus containing cells selected from total population using Hoechst; (c) Leukocytes selected from nucleated cells based on CD45 antigen expression; (d) Cells expressing Ly6G, CD3, CD19, NK1.1 antigens (DUMP+) selected from the CD45+ population and excluded from the analysis; (e) DUMP negative population selected for the expression of CD11b and F4/80 antigens; (f) DUMP- population selected for the expression of Trem2 antigen; (g) Trem2+ population selected for the expression of FITC (liposome); (h) nucleated cells sorted for CD11b expression; (i) nucleated cells selected for F4/80 antigen.

and macrophages. Furthermore, there is a noticeable variation between T6P and empty liposomes, starting from Population B uptake.

Additionally, liposome-positive KCs, MoMFs, and macrophages were analyzed from the KCs flow panel (Figure 4.15). MoMFs had more positive events. Macrophages show the lowest uptake, whereas KCs reach roughly 30%.

As debated in Paragraph 4.3.3, the panels for LAMs and KCs demonstrated distinct CD45+ populations, with the second dataset exhibiting significantly lower levels. As a result, it is not feasible to directly compare the data between KC and LAM populations. Consequently,
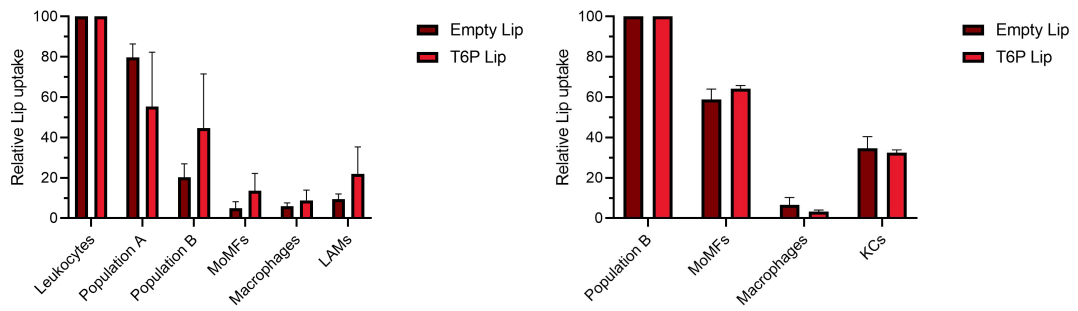
FIGURE 4.15: Percent positive populations for T6P liposome uptake. On the left, focus on treatment positive LAMs. On the right, uptake from KCs.

the liposome uptake by these two cell subsets cannot be reliably compared.

4.3.4 Immunohistochemical staining

work in progress

4.4 FcGR1 liposomes

The FcGR1 liposome was synthesized following Szachniewicz's work where it was previously assessed in [56]. His synthesized particles had Prednisolone phosphate (PLP) as cargo, a gluco-corticoid drug. He performed an animal efficacy study and found promising results, derived from decreased expression of pro-inflammatory surface markers (CD14, FcR1) and augmented anti-inflammatory surface markers (CX3CR1, CD206). In this current project, minor modifications were made on the formulation by neglecting the cargo and employing different dyes for the biodistribution analysis. In addition, Szachniewicz conducted conjugation efficiency tests for FcGR1 liposomes and performed stability assays. However, these assessments were not included in the analysis due to time constraints.

In Figure 4.16, the used treatment and control particles are shown. Their center is the aqueous core, the yellow lipid bilayer is made of DPPC.
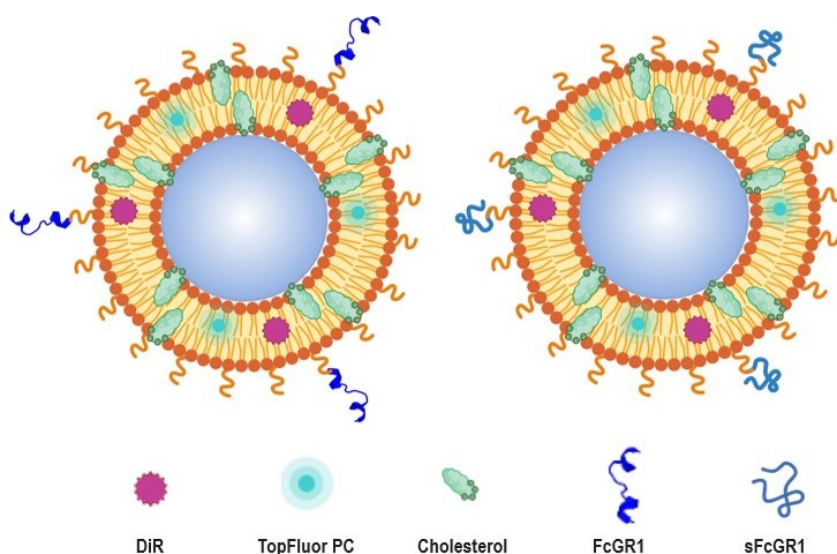

FIGURE 4.16: Model of the synthesized liposomes. On the right, the FcGR1 particle is showed with FcGR1 azide marked in blue, on the surface with PEG chains in orange. In the bilayer, TopFluor PC in light blue, cholesterol in green and DiR in lilac are displayed. On the left side, the control liposome has the scrambled peptide.

4.4.1 Characterization of liposomes

The liposomes were characterized for diameter, PDI and zeta potential. DLS was used to analyze sFcGR1 and FcGR1 liposome (Table 4.4). The formulations were extruded through membranes that have 200 and 100nm cutoff. Both particles greatly exceed these values, probably due to low stability and aggregation. While FcGR1 formulation presented a single-peaked and moderately polydispersed size distribution, the control showed a broadly polydispersed distribution (PdI > 0.4) with more than one peak.

Furthermore, it is relevant to remind that the conjugated component FcGR1 refers to a protein, namely (6-Azido)-KLRSQECDWEEISVK, able to specifically bind FcγR1 receptors. Secondly, the treatement surface charge is more negatively charged than the control. This may due some peptides, in the (6-Azido)-KLRSQECDWEEISVK chain, that have carboxyl groups on their side chains. These are negatively charged at physiological pH, probably their influence is dimmed in the scrambled version of the protein that is in the control formulation. A complete biodistribution panel is shown in the Appendix (Figure

7.7).

Liposomes	Size by number in PBS (d.nm ± SD)	Polydispersity index (PdI ± SD)	ζ potential in KCl (mV ± SD)
sFcGR1 Lip	303.7 ± 4.5	0.39 ± 0.01	-3.82 ± 0.70
FcGR1 Lip	358.8 ± 67.7	0.88 ± 0.05	-17.80 ± 0.89

TABLE 4.4: Size and zeta potential of FcGR1 and control liposomes. In the size distribution of the treatment, there was one single peak, the reported size derives from it. Z-avg fit was used for the control instead.

In the previous theses that dealt with the assessed liposomes, no abnormal particle sizes were found during the characterization process.
4-OI crystalizes at 4°C, this property was not taken into account during liposome preparation. As a matter of fact, dialysis was performed at 4°C instead of RT. This surely affected 4-OI liposome size by deteriorating 4-OI integration in the DPPC bilayer [60].

Secondly, Szachniewicz included a drug molecule (PLP) as a cargo in his formulations. As a control, he had a T6P liposome without drug and a FcGR1 liposome without drug. Furthermore, Szachniewicz dialyzed T6-P and FcGR1 formulations for 5 days with daily buffer changes [56]. Instead, within this biodistribution study, the liposomes were in dialysis for 24h.

Moreover, Bartneck at al. analyzed dexamethasone-loaded liposome within a NASH biodistribution study. Interestingly, they used a formulation remarkably close to the one employed during this study. They prepared a mix of chloroform and methanol including DPPC: DSPE-PEG: Cholesterol at a molar% of 61.6:5:33.3. A size of 100nm was reported [5].

4.4.2   In vivo biodistribution study

To investigate the in vivo organ distribution of FcGR1 liposome in C57BL/6J mice, the lipophilic DiR fluorescent dye was utilized for near-infrared (NIR) imaging. Mice were treated with 150 µL of sFcGR1 and FcGR1 liposomes. The signals were captured using the PEARL Trilogy whole-animal NIR imaging system.
Figure 4.17 shows on the right representative pictures of the different groups at 1h, 4h and 24h. Both liposomes display a contained and similar liver localization over time. The control mice exhibit a slightly increased absorption in proximity to the spleen. The FcGR1 sample provides a marginally higher fluorescent signal than the control, while having a peak at 24h post IV injection.
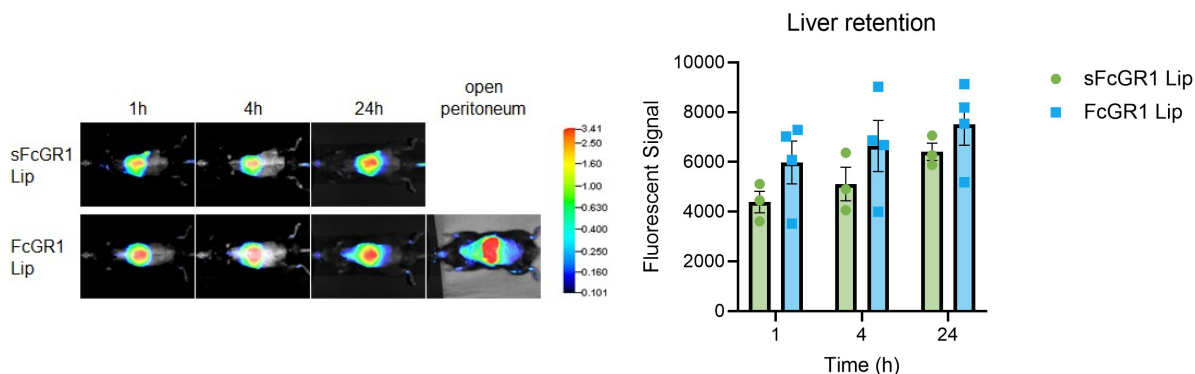
FIGURE 4.17: On the left, a representative in vivo localization images for each treatment condition at 1h, 4h and 24h time points. On the right side, a plot showing quantification of signal localized in the liver region for both liposomes at 1h, 4h and 24h time point.

In Figure 4.18, the retention signal from heart, liver, kidneys, lungs and spleen is presented. The organs were placed by following the scheme shown in Figure 3.3. The absorption of both liposomes in the liver appears to be elevated and equal. The remaining organs show poor retention levels, with the exception of the spleen, which exhibits a minor uptake in both conditions.
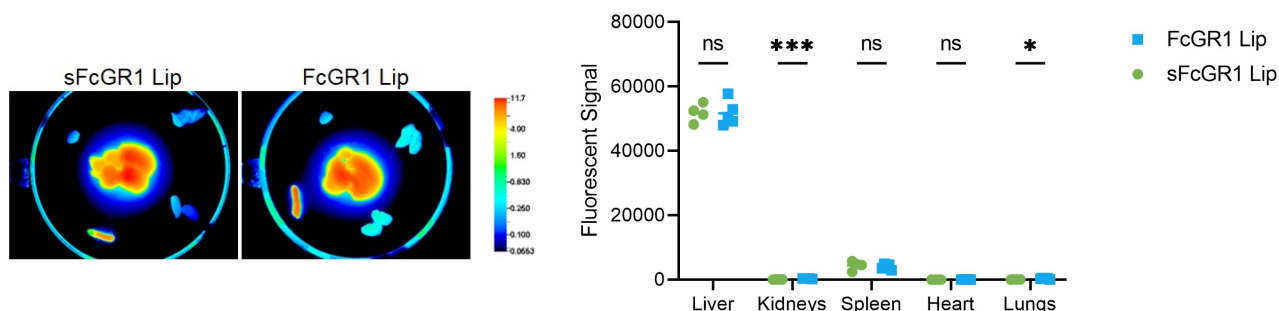

FIGURE 4.18: On the left, a representative image of fluorescent signal in excised organs from control and treatment conditions. In the center lays the liver, on the top right and then clockwise there are: lungs, kidneys, spleen and heart. On the right, it is plotted a relative localization of fluorescent signal in the excised organs.

4.4.3 FACS analysis of liver samples

See Paragraph 4.1.3, as the gating procedure was unchanged. In addition, the hierarchy scheme is available in Figure 4.5 for LAMs panel.

The samples treated with FcGR1 liposome showed inconsistent results when compared to T6P data, regarding LAMs panel. The results deriving from FcGR1-related samples present significant variations in staining performance (Figure 4.19), likely due to some batch to batch disparity. In Figure 4.19, (c) shows a very poor CD45 positive population among nucleated cells. Unfortunately, this output jeopardizes every cell subsets placed below the hierarchy chain. Therefore, DUMP negative events (d) are quite limited, macrophage recognition is also less effective. However, MoMFs and macrophages are two
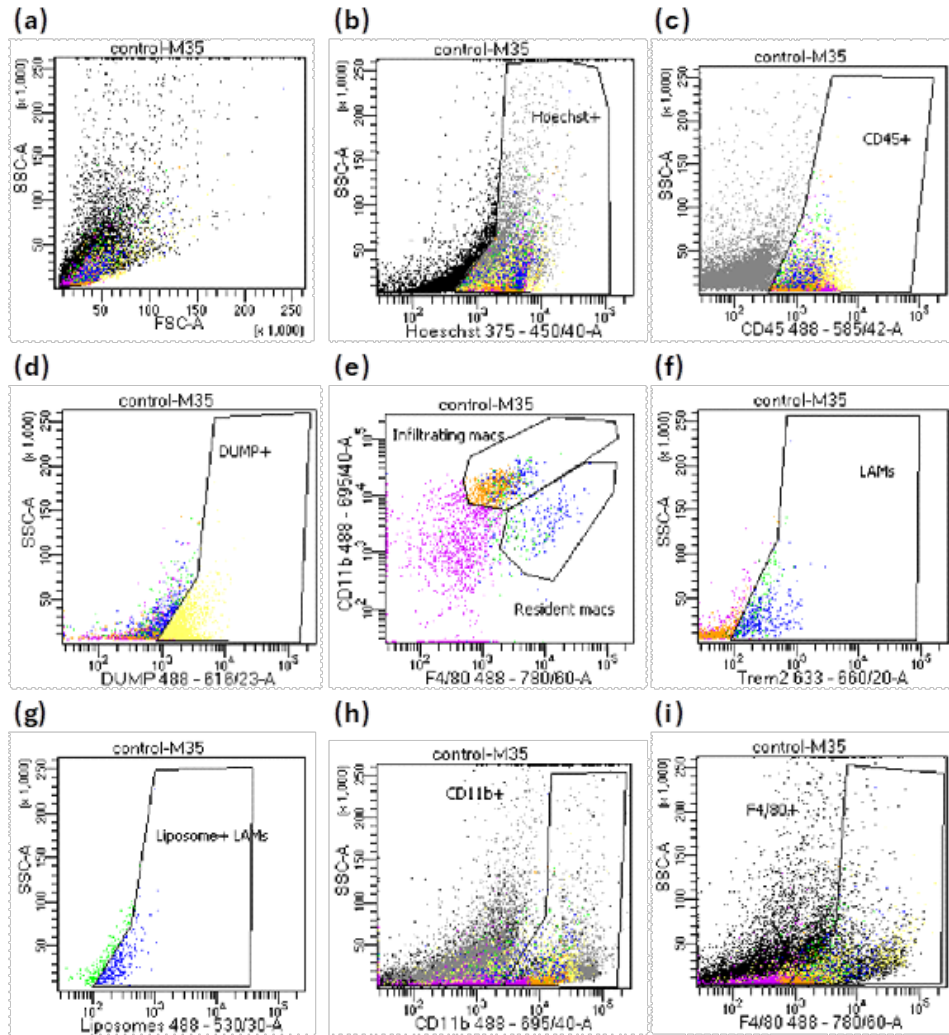
FIGURE 4.19: Populations positive for respective antigen expression plotted on fluorophore spectrum: (a) Side scatter vs forward scatter of all cells visualized; (b) Nucleus containing cells selected from total population using Hoechst; (c) Leukocytes selected from nucleated cells based on CD45 antigen expression; (d) Cells expressing Ly6G, CD3, CD19, NK1.1 antigens (DUMP+) selected from the CD45+ population and excluded from the analysis; (e) DUMP negative population selected for the expression of CD11b and F4/80 antigens; (f) DUMP- population selected for the expression of Trem2 antigen; (g) Trem2+ population selected for the expression of FITC (liposome); (h) nucleated cells sorted for CD11b expression; (i) nucleated cells selected for F4/80 antigen.

discernible populations (e). Furthermore, (f) does not exhibit any shift with Trem2 positive events, possibly due to low CD45+ cells or inefficient antibody binding. The hierarchy for this panel is shown in Figure 7.10 in the Appendix.

Secondly, a flow panel to identify KCs was employed. The results are considerably consistent with T6P-associated data from LAMs panel. Thus, related delucidations are discussed in the final part of Paragraph 4.3.3. Additional pictures are available in the Appendix (Figure 7.10 and 7.11).

Lastly, flow cytometry results for LSECs were not included in the results of this thesis,

as they were deemed less relevant to the primary focus on macrophage-targeted liposomal uptake.

An inadequate FITC signal was common in every flow panel that was analyzed. In all the flow cytometry data representing FITC, there was not any recognizable population that was positive for liposomes. As almost every sorted cell population were assessed for FITC expression, this issue was confirmed not to be population-specific.
In addition, control liposome of T6P group showed close to optimal size (132nm) (Table 4.3), there was no significant improvement in FITC expression in the flow results. Then it was not a group-specific issue. Rather a constant and structural limitation caused by some sort of incompatibility between TopFluor PC dye and the studied formulations.

Münter et al synthesized DSPE liposomes and assessed fluorescently labeled lipids dissociation in plasma. Among other tags, they also analyzed TopFluor PC and found high dissociation rates (40%). Where, 50% dissociation corresponds to all fluorescently labeled lipids in the outer leaflet of the liposomal membrane, and thus the entire fluorophore pool being accessible for the surrounding environment. It is reported that, a combination of bulky fluorescent group and molecule orientation may force TopFluor PC to have an energetically unfavorable position position in the liposome hydrophobic bilayer, thus causing potential disruptions [42].

Differential uptake of treatment As stated in Paragraph 3.7, the liposome signal (FITC probe) was recorded for cell sets and subsets sorted across various flow panels. Population A consists of CD45+DUMP+ cells, while Population B includes CD45+DUMP- cells, representing macrophages and monocytes. The ratio of liposome-positive events for these groups was compared to liposome-positive leukocytes (CD45+ cells).
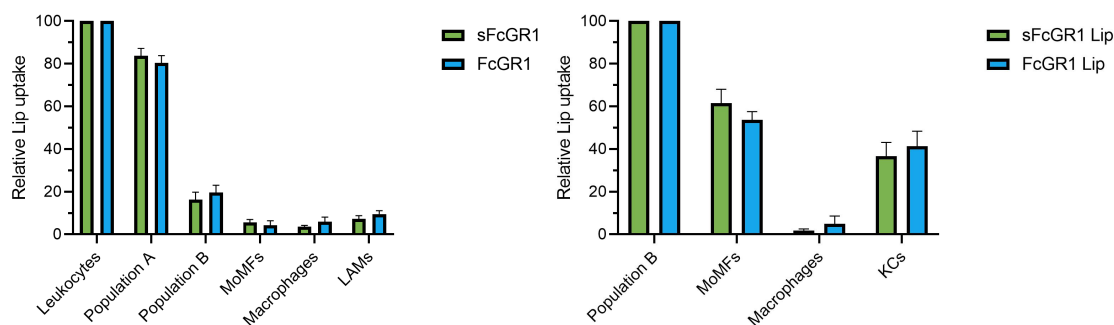

FIGURE 4.20: Percent positive populations for FcGR1 liposome uptake. On the left, focus on treatment positive LAMs. On the right, uptake from KCs.

Focusing on Population B, data for liposome-positive MoMFs, macrophages, and LAMs were obtained from the LAMs flow panel, with percentages relative to treatment-positive Population B.
The left plot shows a minimal and comparative uptake from all three macrophage subsets. This is a consequence of the negligible CD45+ and DUMP- population that resulted from LAMs panel (Figure 4.19).
Additionally, liposome-positive KCs, MoMFs, and macrophages were analyzed from the KCs flow panel (Figure 4.20). MoMFs had more positive events. KCs show approximately 40% uptake and macrophage lovwer than 5%.

The panels for LAMs and KCs demonstrated distinct CD45+ populations, with the second dataset exhibiting significantly lower levels. As a result, it is not feasible to directly compare the data between KC and LAM populations. Consequently, the liposome uptake by these two cell subsets cannot be reliably compared.

4.4.4 Immunohistochemical staining

work in progress

Chapter 5

Conclusions and future work

The primary aim of this thesis—to examine the in vivo and cellular distribution of liposomal formulations in a MASLD mouse model—was successfully achieved. In detail, multiple liposome formulations were prepared and characterize by following previous protocols. The size and PDI results were not optimal. As the hypotheses overlap with the missing objectives (Paragraph 2.1), hypotheses are discussed next.
Additionally, the first hypothesis-preferential uptake of the liposomal formulations by the liver-was confirmed, demonstrating that all liposomal formulations exhibit major uptake in the liver. However, the remaining hypotheses could not be conclusively addressed due to multiple reasons.
With respect to the second hypothesis-increased uptake by macrophages-liposome positive cells were exclusively examined within macrophage subpopulations. Thus preventing the opportunity of having a control cell population (LSECs) whose treatment uptake could be assessed and compared to macrophages.
Regarding the presumed preferential uptake by LAMs, inconsistencies in the flow cytometry data prevented meaningful comparisons between LAMs and KCs uptake, precluded the ability to draw definitive conclusions. On the other hand, the flow panels can be examined independently for each formulation.
From Figure 4.6 related to DHA-CS liposome, there is an equivalent uptake from MoMFs and LAMs. Whereas, the right plot shows an increased MoMFs populations positive to liposomes when compared to KCs. Figure 4.10, related to 4-OI liposome, presents a cell uptake profile that is equal to the DHA-CS liposome.
Moreover, from Figure 4.15 related to T6P liposome, LAMs uptake is slightly higher than MoMFs. The right panel shows much higher treatment positive MoMFs when compared with KCs. Figure 4.20, related to FcGR1 liposome, shows very similar results to the T6P formulation.

One critical observation from FACS results was the high variability between experimental batches. This variability underscores the importance of optimizing sample preparation protocols. A potential improvement involves performing all sample stainings in a single session, even if the flow readings are conducted on separate days, to minimize inconsistencies. Simplifying the workflow for flow cytometry preparation is also recommended, including preliminary in vitro experiments with mouse immune cell lines such as 3T3 or LX-2. These models can be used to test antibody performance by evaluating signal intensity and event counts, enabling the selection of higher-quality antibodies and improving overall experimental reliability.

Furthermore, advancing the synthesis of liposomal formulations with rigorous controls is vital. These controls should closely match the formulations previously tested in the previous studies to ensure consistency and comparability. For example, excluding TopFluor PC from formulations may help address discrepancies and provide more accurate data for future therapeutic development.

Chapter 6

Future outlook

The development of macrophage-targeted therapies holds great promise for addressing the complex pathophysiology of MASH. LAMs represent a particularly attractive target due to their critical role in modulating inflammation. Harnessing their potential through therapeutic strategies, such as conditioning their phenotype or enhancing their reparative functions, could yield significant advancements in MASH treatment. Alternatively, designing lipid nanoparticles that selectively target such specific macrophage subsets offers a novel and potentially more precise approach to mitigating liver inflammation and fibrosis. Given the substantial burden of severe comorbidities, including cardiovascular disease and diabetes, that often accompany MASH, the impact of innovative therapies cannot be overstated. This highlights the urgent need for continued research and the translation of these promising strategies into clinically viable solutions for MASH management.

Chapter 7

Appendix

7.1 Synthesis of control formulations

DHA Lip	Molecular weight (g/mol)	Mol%	mg in 0.3ml
DPPC	733.56	57.00	4.94
DHA	328.49	20.00	0.78
Cholesterol	386.65	20.00	0.91
Cholesterol sulfate Na	488.70	0.00	0.00
DSPE PEG	2803.78	2.00	0.66
DSPE PEG Cy7	3302.09	0.50	0.21
TopFluor PC	909.97	0.50	0.12

TABLE 7.1: Composition of DHA Liposomes, the control formulation of DHA-CS liposomes.

Empty Lip	Molecular weight (g/mol)	Mol%	mg in 0.4ml
4-OI	242.31	0.00	0.00
DPPC	733.56	65.00	10.39
Cholesterol	488.70	32.00	3.41
DSPE PEG	3077.80	2.00	1.34
DSPE PEG Cy7	3302.09	0.50	0.36
TopFluor PC	909.97	0.50	0.16

TABLE 7.2: Composition of Empty Liposomes, the control formulation of the 4-OI liposomes.

Empty Lip	Molecular weight (g/mol)	Mol%	mg in 0.5ml
DPPC	733.56	56.50	33.38
DPPG	744.95	3.00	1.80
Cholesterol	386.65	40.00	12.46
T6P	580.71	0.00	0.00
DiR	1013.40	0.50	0.40
TopFluor PC	909.97	0.50	0.41

TABLE 7.3: The Empty Liposome composition is the control group of the T6P formulation.

sFcGR1 Lip	Molecular weight (g/mol)	Mol%	mg in 0.5ml
DPPC	733.56	57.00	16.22
Cholesterol	386.65	40.00	6.00
FcGR1 azide	1989.09	0.00	0.00
scrambled FcGR1 azide	1989.09	1.92	0.75
DSPE PEG DBCO	3077.80	2.50	2.99
DiR	1013.40	1.00	0.40
TopFluor PC	909.97	0.50	0.20

TABLE 7.4: sFcGR1 Liposome composition. This formulation is the control group of the FcGR1 liposomes.

7.2 In vivo biodistribution study
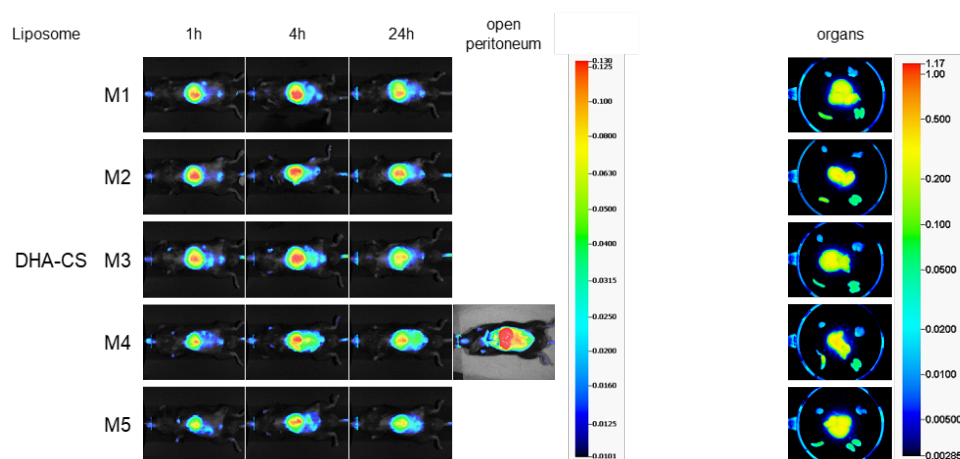
7.2.1 DHA-CS liposome

FIGURE 7.1: Biodistribution images and analysis of whole body at 1, 4 and 24 hours, and organs at 24 hours
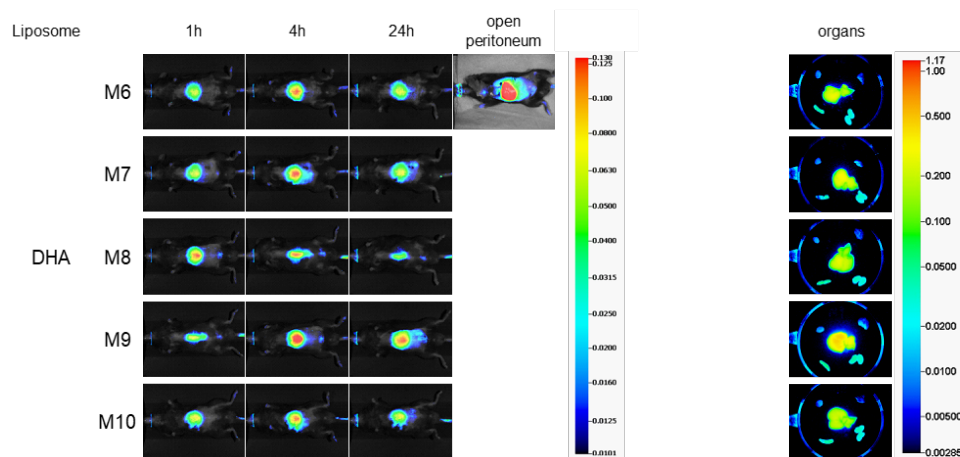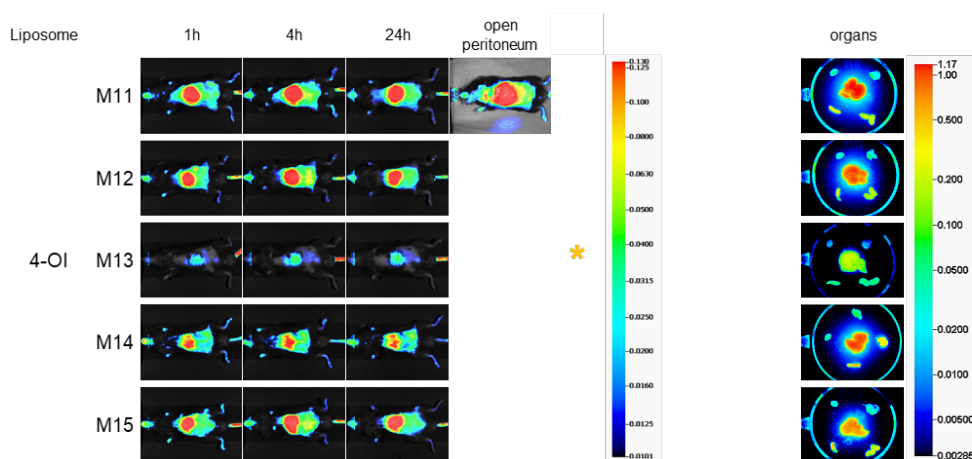
FIGURE 7.2: Biodistribution images and analysis of whole body at 1, 4 and 24 hours, and organs at 24 hours

7.2.2 4-OI liposome

FIGURE 7.3: Biodistribution images and analysis of whole body at 1, 4 and 24 hours, and organs at 24 hours
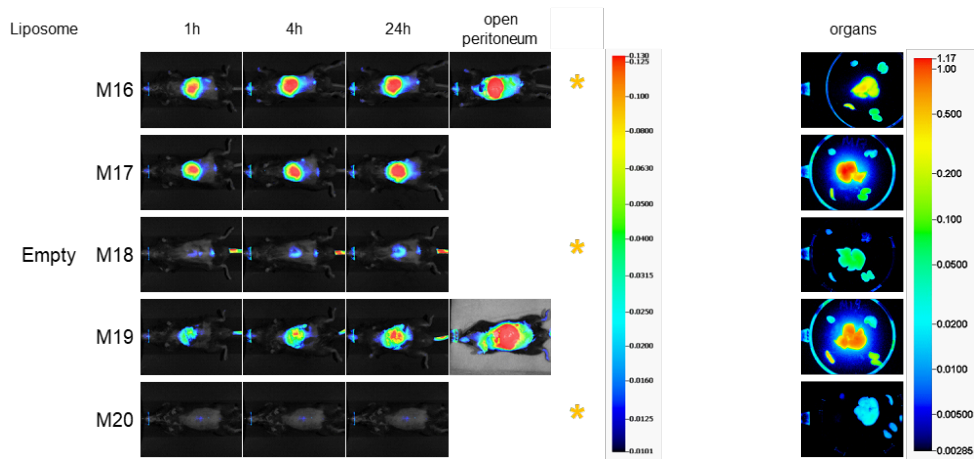
FIGURE 7.4: Biodistribution images and analysis of whole body at 1, 4 and 24 hours, and organs at 24 hours
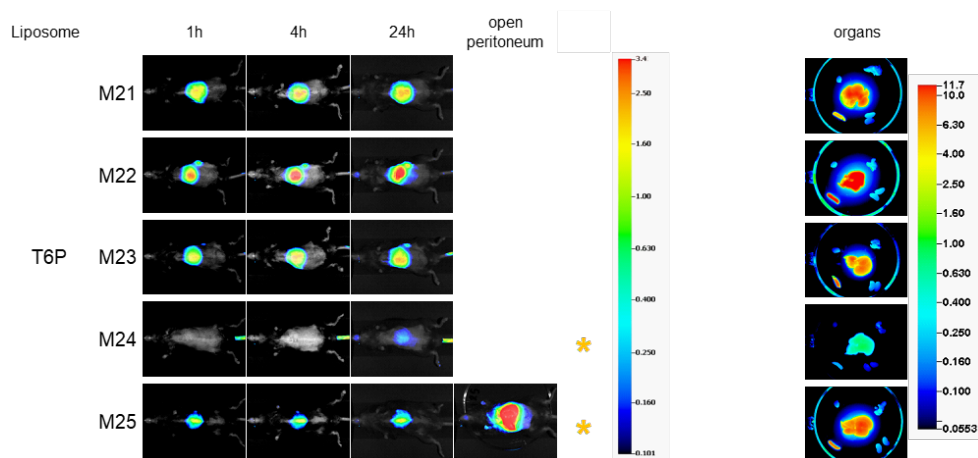
7.2.3 T6P liposome

FIGURE 7.5: Biodistribution images and analysis of whole body at 1, 4 and 24 hours, and organs at 24 hours
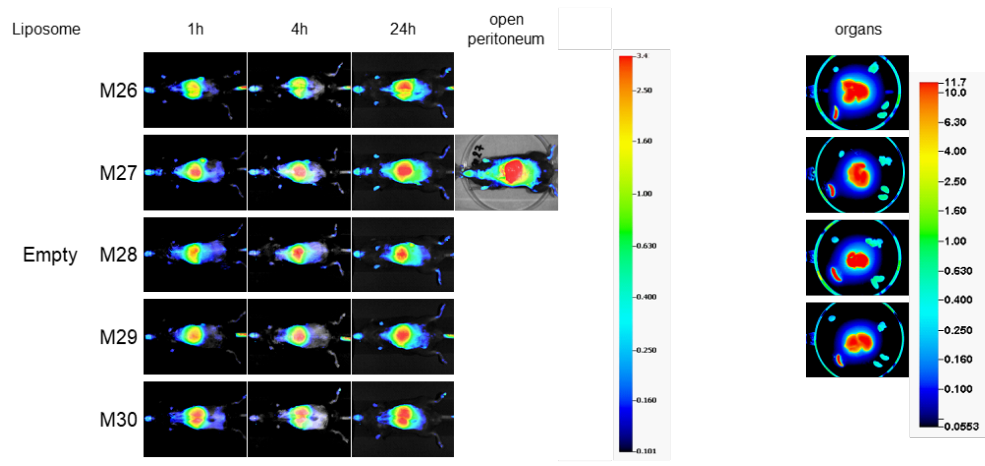
FIGURE 7.6: Biodistribution images and analysis of whole body at 1, 4 and 24 hours, and organs at 24 hours
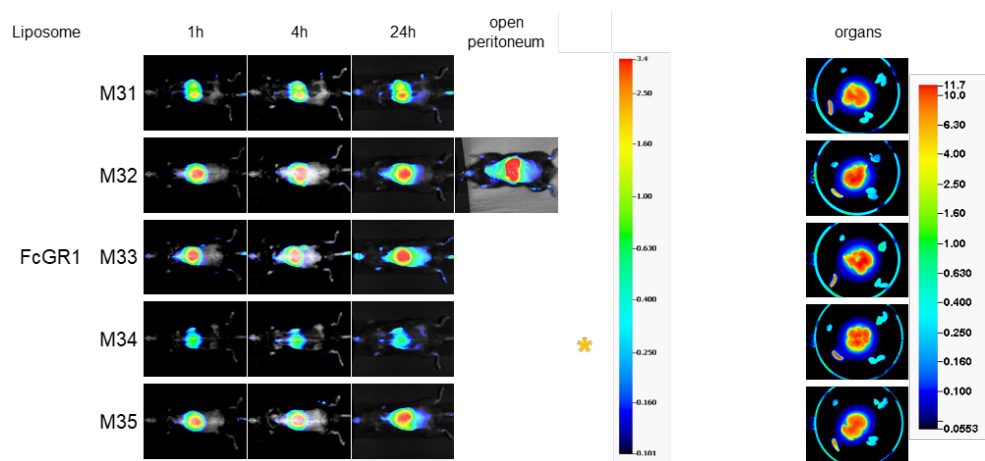
7.2.4 FcGR1 liposome

FIGURE 7.7: Biodistribution images and analysis of whole body at 1, 4 and 24 hours, and organs at 24 hours
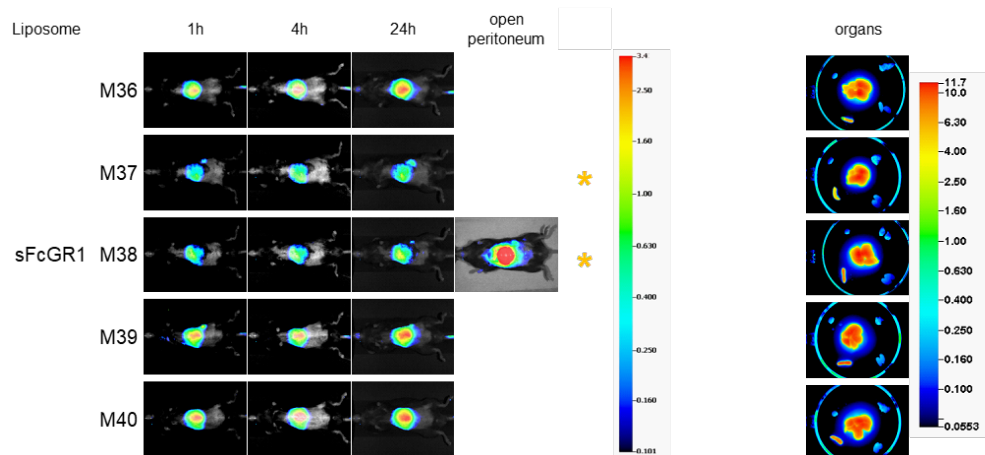
FIGURE 7.8: Biodistribution images and analysis of whole body at 1, 4 and 24 hours, and organs at 24 hours

7.3 Flow panels

FIGURE 7.9: Populations positive for respective antigen expression plotted on fluorophore spectrum: (a) Leukocytes selected from nucleated cells based on CD45 antigen expression; (b) Cells expressing Ly6G, CD3, CD19, NK1.1 antigens (DUMP+) selected from the CD45+ population and excluded from the analysis; (c) DUMP negative population selected for the expression of CD11b and F4/80 antigens; (d) DUMP- population selected for the expression of Tim4 antigen; (e) Tim4+ population selected for the expression of FITC (liposome).

FIGURE 7.10: Gating hierarchy employed for KCs identification for cells derived from mice liver from biodistribution study.
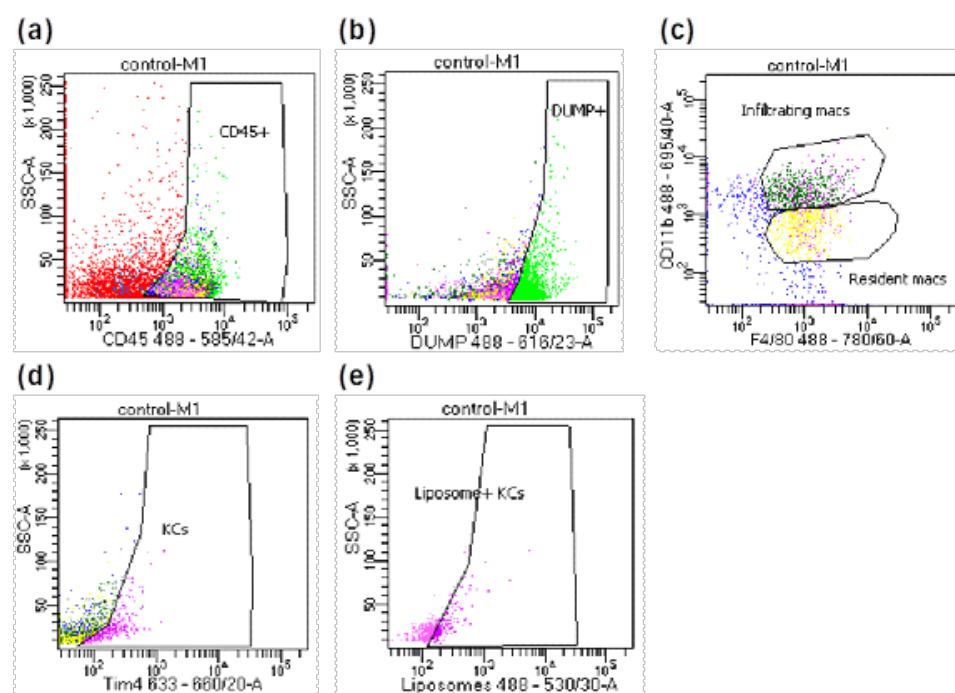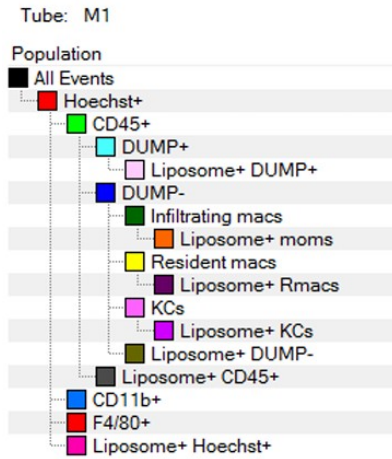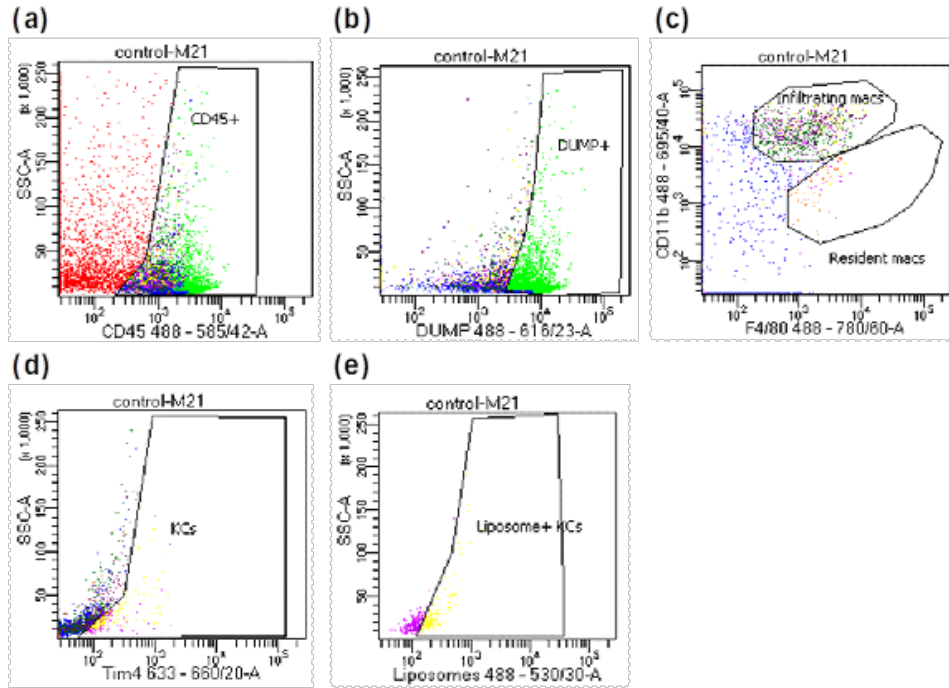

FIGURE 7.11: Populations positive for respective antigen expression plotted on fluorophore spectrum: (a) Leukocytes selected from nucleated cells based on CD45 antigen expression; (b) Cells expressing Ly6G, CD3, CD19, NK1.1 antigens (DUMP+) selected from the CD45+ population and excluded from the analysis; (c) DUMP negative population selected for the expression of CD11b and F4/80 antigens; (d) DUMP- population selected for the expression of Tim4 antigen; (e) Tim4+ population selected for the expression of FITC (liposome).

Bibliography

[1] Zeinab Abdullah and Percy A Knolle. Liver macrophages in healthy and diseased liver. *Pflügers Archiv-European Journal of Physiology*, 469(3):553–560, 2017.

[2] Alejandra Altamirano-Barrera, Beatriz Barranco-Fragoso, and Nahum Méndez-Sánchez. Management strategies for liver fibrosis. *Annals of hepatology*, 16(1):48–56, 2017.

[3] Paras K Anand. Lipids, inflammasomes, metabolism, and disease. *Immunological Reviews*, 297(1):108–122, 2020.

[4] Angelo Armandi and Elisabetta Bugianesi. Dietary and pharmacological treatment in patients with metabolic-dysfunction associated steatotic liver disease. *European Journal of Internal Medicine*, 2024.

[5] Matthias Bartneck, Katharina M Scheyda, Klaudia T Warzecha, Larissa Y Rizzo, Kanishka Hittatiya, Tom Luedde, Gert Storm, Christian Trautwein, Twan Lammers, and Frank Tacke. Fluorescent cell-traceable dexamethasone-loaded liposomes for the treatment of inflammatory liver diseases. *Biomaterials*, 37:367–382, 2015.

[6] Lynette Beattie, Amy Sawtell, Jason Mann, Teija CM Frame, Bianca Teal, Fabian de Labastida Rivera, Najmeeyah Brown, Katherine Walwyn-Brown, John WJ Moore, Sandy MacDonald, et al. Bone marrow-derived and resident liver macrophages display unique transcriptomic signatures but similar biological functions. *Journal of hepatology*, 65(4):758–768, 2016.

[7] Valentina Bianco, Melanie Korbelius, Nemanja Vujic, Alena Akhmetshina, Melina Amor, Dagmar Kolb, Anita Pirchheim, Ivan Bradic, Katharina B Kuentzel, Martin Buerger, et al. Impact of (intestinal) lal deficiency on lipid metabolism and macrophage infiltration. *Molecular metabolism*, 73:101737, 2023.

[8] Wah-Kheong Chan, Kee-Huat Chuah, Ruveena Bhavani Rajaram, Lee-Ling Lim, Jeyakantha Ratnasingam, and Shireene Ratna Vethakkan. Metabolic dysfunction-associated steatotic liver disease (masld): a state-of-the-art review. *Journal of Obesity & Metabolic Syndrome*, 32(3):197, 2023.

[9] Sabine Daemen, Anastasiia Gainullina, Gowri Kalugotla, Li He, Mandy M Chan, Joseph W Beals, Kim H Liss, Samuel Klein, Ariel E Feldstein, Brian N Finck, et al. Dynamic shifts in the composition of resident and recruited macrophages influence tissue remodeling in nash. *Cell reports*, 34(2), 2021.

[10] Lindsey Devisscher, Charlotte L Scott, Sander Lefere, Sarah Raevens, Eliene Bogaerts, Annelies Paridaens, Xavier Verhelst, Anja Geerts, Martin Guilliams, and Hans Van Vlierberghe. Non-alcoholic steatohepatitis induces transient changes within the liver macrophage pool. *Cellular immunology*, 322:74–83, 2017.

[11] Peter Dietrich and Claus Hellerbrand. Non-alcoholic fatty liver disease, obesity and the metabolic syndrome. *Best practice & research Clinical gastroenterology*, 28(4):637–653, 2014.

[12] Hannah K Drescher, Sabine Weiskirchen, and Ralf Weiskirchen. Current status in testing for nonalcoholic fatty liver disease (nafld) and nonalcoholic steatohepatitis (nash). *Cells*, 8(8):845, 2019.

[13] Jeremy S Duffield, Stuart J Forbes, Christothea M Constandinou, Spike Clay, Marina Partolina, Srilatha Vuthoori, Shengji Wu, Richard Lang, John P Iredale, et al. Selective depletion of macrophages reveals distinct, opposing roles during liver injury and repair. *The Journal of clinical investigation*, 115(1):56–65, 2005.

[14] Hila Epstein-Barash, Dikla Gutman, Ela Markovsky, Galit Mishan-Eisenberg, Nickolay Koroukhov, Janos Szebeni, and Gershon Golomb. Physicochemical parameters affecting liposomal bisphosphonates bioactivity for restenosis therapy: internalization, cell inhibition, activation of cytokines and complement, and mechanism of cell death. *Journal of controlled release*, 146(2):182–195, 2010.

[15] Pedro L Esquinas, Ajit Shinto, Koramadai K Kamaleshwaran, Jephy Joseph, and Anna Celler. Biodistribution, pharmacokinetics, and organ-level dosimetry for 188 re-ahdd-lipiodol radioembolization based on quantitative post-treatment spect/ct scans. *EJNMMI physics*, 5:1–22, 2018.

[16] Thomas Fabre, Alexander MS Barron, Stephen M Christensen, Shoh Asano, Kathryn Bound, Matthew P Lech, Marc H Wadsworth, Xiao Chen, Chang Wang, Ju Wang, et al. Identification of a broadly fibrogenic macrophage subset induced by type 3 inflammation. *Science immunology*, 8(82):eadd8945, 2023.

[17] Ferdinand Fandrei, Oskar Engberg, Lukáš Opálka, Pavla Jančálková, Petra Pullmannová, Miloš Steinhart, Andrej Kováčik, Kateřina Vávrová, and Daniel Huster. Cholesterol sulfate fluidizes the sterol fraction of the stratum corneum lipid phase and increases its permeability. *Journal of Lipid Research*, 63(3), 2022.

[18] National Center for Biotechnology Information. Pubchem compound summary for cid 15071718, alpha,alpha'-trehalose 6-palmitate. Online Database, 2025. Retrieved January 14, 2025, from `https://pubchem.ncbi.nlm.nih.gov/compound/alpha_alpha_-Trehalose-6-palmitate`.

[19] Sven Francque, Gyongyi Szabo, Manal F Abdelmalek, Christopher D Byrne, Kenneth Cusi, Jean-François Dufour, Michael Roden, Frank Sacks, and Frank Tacke. Nonalcoholic steatohepatitis: the role of peroxisome proliferator-activated receptors. *Nature reviews Gastroenterology & hepatology*, 18(1):24–39, 2021.

[20] Scott L Friedman, Vlad Ratziu, Stephen A Harrison, Manal F Abdelmalek, Guruprasad P Aithal, Juan Caballeria, Sven Francque, Geoffrey Farrell, Kris V Kowdley, Antonio Craxi, et al. A randomized, placebo-controlled trial of cenicriviroc for treatment of nonalcoholic steatohepatitis with fibrosis. *Hepatology*, 67(5):1754–1767, 2018.

[21] Martin Guilliams and Charlotte L Scott. Liver macrophages in health and disease. *Immunity*, 55(9):1515–1529, 2022.

[22] Stephen A Harrison, Pierre Bedossa, Cynthia D Guy, Jörn M Schattenberg, Rohit Loomba, Rebecca Taub, Dominic Labriola, Sam E Moussa, Guy W Neff, Mary E Rinella, et al. A phase 3, randomized, controlled trial of resmetirom in nash with liver fibrosis. *New England Journal of Medicine*, 390(6):497–509, 2024.

[23] Tim Hendrikx, Florentina Porsch, Máté G Kiss, Dragana Rajcic, Nikolina Papac-Miličević, Constanze Hoebinger, Laura Goederle, Anastasiya Hladik, Lisa E Shaw, Hauke Horstmann, et al. Soluble trem2 levels reflect the recruitment and expansion of trem2+ macrophages that localize to fibrotic areas and limit nash. *Journal of hepatology*, 77(5):1373–1385, 2022.

[24] Justin R Henning, Christopher S Graffeo, Adeel Rehman, Nina C Fallon, Constantinos P Zambirinis, Atsuo Ochi, Rocky Barilla, Mohsin Jamal, Michael Deutsch, Stephanie Greco, et al. Dendritic cells limit fibroinflammatory injury in nonalcoholic steatohepatitis in mice. *Hepatology*, 58(2):589–602, 2013.

[25] Noelle A Hutchins, Chun-Shiang Chung, Joshua N Borgerding, Carol A Ayala, and Alfred Ayala. Kupffer cells protect liver sinusoidal endothelial cells from fas-dependent apoptosis in sepsis by down-regulating gp130. *The American journal of pathology*, 182(3):742–754, 2013.

[26] Samar H Ibrahim, Rohit Kohli, and Gregory J Gores. Mechanisms of lipotoxicity in nafld and clinical implications. *Journal of pediatric gastroenterology and nutrition*, 53(2):131–140, 2011.

[27] Paola Italiani and Diana Boraschi. From monocytes to m1/m2 macrophages: phenotypical vs. functional differentiation. *Frontiers in immunology*, 5:514, 2014.

[28] Ayaka Iwata, Juri Maruyama, Shibata Natsuki, Akira Nishiyama, Tomohiko Tamura, Minoru Tanaka, Shigeyuki Shichino, Takao Seki, Toshihiko Komai, Tomohisa Okamura, et al. Egr2 drives the differentiation of ly6chi monocytes into fibrosis-promoting macrophages in metabolic dysfunction-associated steatohepatitis in mice. *Communications Biology*, 7(1):681, 2024.

[29] Diego Adhemar Jaitin, Lorenz Adlung, Christoph A Thaiss, Assaf Weiner, Baoguo Li, Hélène Descamps, Patrick Lundgren, Camille Bleriot, Zhaoyuan Liu, Aleksandra Deczkowska, et al. Lipid-associated macrophages control metabolic homeostasis in a trem2-dependent manner. *Cell*, 178(3):686–698, 2019.

[30] Craig N Jenne and Paul Kubes. Immune surveillance by the liver. *Nature immunology*, 14(10):996–1006, 2013.

[31] Dakota R Kamm and Kyle S McCommis. Hepatic stellate cells in physiology and pathology. *The Journal of physiology*, 600(8):1825–1837, 2022.

[32] Susan J Keam. Resmetirom: First approval. *Drugs*, pages 1–7, 2024.

[33] Ciara Kelly, Caroline Jefferies, and Sally-Ann Cryan. Targeted liposomal drug delivery to monocytes and macrophages. *Journal of drug delivery*, 2011(1):727241, 2011.

[34] Oliver Krenkel and Frank Tacke. Macrophages in nonalcoholic fatty liver disease: a role model of pathogenic immunometabolism. In *Seminars in liver disease*, volume 37, pages 189–197. Thieme Medical Publishers, 2017.

[35] Maria Laura Immordino, Franco Dosio, and Luigi Cattel. Stealth liposomes: review of the basic science, rationale, and clinical applications, existing and potential. *International journal of nanomedicine*, 1(3):297–315, 2006.

[36] Cynthia Lebeaupin, Deborah Vallée, Younis Hazari, Claudio Hetz, Eric Chevet, and Béatrice Bailly-Maitre. Endoplasmic reticulum stress signalling and the pathogenesis of non-alcoholic fatty liver disease. *Journal of hepatology*, 69(4):927–947, 2018.

[37] Imke Liebold, Simon Meyer, Markus Heine, Anastasia Kuhl, Jennifer Witt, Leah Eissing, Alexander W Fischer, Anja Christina Koop, Johannes Kluwe, Julian Schulze zur Wiesch, et al. Trem2 regulates the removal of apoptotic cells and inflammatory processes during the progression of nafld. *Cells*, 12(3):341, 2023.

[38] Sonya A MacParland, Jeff C Liu, Xue-Zhong Ma, Brendan T Innes, Agata M Bartczak, Blair K Gage, Justin Manuel, Nicholas Khuu, Juan Echeverri, Ivan Linares, et al. Single cell rna sequencing of human liver reveals distinct intrahepatic macrophage populations. *Nature communications*, 9(1):4383, 2018.

[39] Alessandro Mantovani, Christopher D Byrne, and Giovanni Targher. Efficacy of peroxisome proliferator-activated receptor agonists, glucagon-like peptide-1 receptor agonists, or sodium-glucose cotransporter-2 inhibitors for treatment of non-alcoholic fatty liver disease: a systematic review. *The lancet Gastroenterology & hepatology*, 7(4):367–378, 2022.

[40] Muralidhara Rao Maradana, Suman Kumar Yekollu, Bijun Zeng, Jonathan Ellis, Andrew Clouston, Gregory Miller, Meghna Talekar, Zaied Ahmed Bhuyan, Sachin Mahadevaiah, Elizabeth E Powell, et al. Immunomodulatory liposomes targeting liver macrophages arrest progression of nonalcoholic steatohepatitis. *Metabolism*, 78:80–94, 2018.

[41] Kenji Morino, Kazufumi Kunimura, Yuki Sugiura, Yoshihiro Izumi, Keisuke Matsubara, Sayaka Akiyoshi, Rae Maeda, Kenichiro Hirotani, Daiji Sakata, Seiya Mizuno, et al. Cholesterol sulfate limits neutrophil recruitment and gut inflammation during mucosal injury. *Frontiers in Immunology*, 14:1131146, 2023.

[42] Rasmus Münter, Kasper Kristensen, Dennis Pedersbæk, Jannik Bruun Larsen, Jens Bæk Simonsen, and Thomas Lars Andresen. Dissociation of fluorescently labeled lipids from liposomes in biological environments challenges the interpretation of uptake studies. *Nanoscale*, 10(48):22720–22724, 2018.

[43] Philip N Newsome, Kristine Buchholtz, Kenneth Cusi, Martin Linder, Takeshi Okanoue, Vlad Ratziu, Arun J Sanyal, Anne-Sophie Sejling, and Stephen A Harrison. A placebo-controlled trial of subcutaneous semaglutide in nonalcoholic steatohepatitis. *New England Journal of Medicine*, 384(12):1113–1124, 2021.

[44] Ming Ni, Jing Zhang, Rebecca Sosa, Hanwen Zhang, Han Wang, Dan Jin, Kaitlyn Crowley, Bita Naini, F Elaine Reed, Ronald W Busuttil, et al. T-cell immunoglobulin and mucin domain-containing protein-4 is critical for kupffer cell homeostatic function in the activation and resolution of liver ischemia reperfusion injury. *Hepatology*, 74(4):2118–2132, 2021.

[45] Hamdi Nsairat, Dima Khater, Usama Sayed, Fadwa Odeh, Abeer Al Bawab, and Walhan Alshaer. Liposomes: Structure, composition, types, and clinical applications. *Heliyon*, 8(5), 2022.

[46] C Nick Pace, Gerald R Grimsley, and J Martin Scholtz. Protein ionizable groups: pk values and their contribution to protein stability and solubility. *Journal of Biological Chemistry*, 284(20):13285–13289, 2009.

[47] Soo-Jeung Park, Josefina Garcia Diaz, Eugene Um, and Young S Hahn. Major roles of kupffer cells and macrophages in nafld development. *Frontiers in Endocrinology*, 14:1150118, 2023.

[48] A.S. Rajan. Metabolic reprogramming of macrophages using liposomal itaconate to resolve nash inflammation. Msc thesis, University of Twente, 2022.

[49] P Ramachandran, R Dobie, JR Wilson-Kanamori, EF Dora, BEP Henderson, NT Luu, JR Portman, KP Matchett, M Brice, JA Marwick, et al. Resolving the fibrotic niche of human liver cirrhosis at single-cell level. *Nature*, 575(7783):512–518, 2019.

[50] Biplab Roy, Pritam Guha, Ravi Bhattarai, Prasant Nahak, Gourab Karmakar, Priyam Chettri, and Amiya Kumar Panda. Influence of lipid composition, ph, and temperature on physicochemical properties of liposomes with curcumin as model drug. *Journal of oleo science*, 65(5):399–411, 2016.

[51] Emma Samuelsson, Haifa Shen, Elvin Blanco, Mauro Ferrari, and Joy Wolfram. Contribution of kupffer cells to liposome accumulation in the liver. *Colloids and Surfaces B: Biointerfaces*, 158:356–362, 2017.

[52] Julian Schwärzler, Felix Grabherr, Christoph Grander, Timon E Adolph, and Herbert Tilg. The pathophysiology of masld: an immunometabolic perspective. *Expert review of clinical immunology*, 20(4):375–386, 2024.

[53] Charlotte L Scott, Fang Zheng, Patrick De Baetselier, Liesbet Martens, Yvan Saeys, Sofie De Prijck, Saskia Lippens, Chloé Abels, Steve Schoonooghe, Geert Raes, et al. Bone marrow-derived monocytes give rise to self-renewing and fully differentiated kupffer cells. *Nature communications*, 7(1):10321, 2016.

[54] Ekihiro Seki, Samuele De Minicis, Geum-Youn Gwak, Johannes Kluwe, Sayaka Inokuchi, Christina A Bursill, Josep M Llovet, David A Brenner, Robert F Schwabe, et al. Ccr1 and ccr5 promote hepatic fibrosis in mice. *The Journal of clinical investigation*, 119(7):1858–1870, 2009.

[55] Michael H Sieweke and Judith E Allen. Beyond stem cells: self-renewal of differentiated macrophages. *Science*, 342(6161):1242974, 2013.

[56] M. M. Szachniewicz. Nanotechnology-based targeted drug delivery systems for treatment of liver fibrosis. Msc thesis, University of Twente, 2017.

[57] Felista L Tansi, Ronny Rüger, Ansgar M Kollmeier, Claudia Böhm, Roland E Kontermann, Ulf K Teichgraeber, Alfred Fahr, and Ingrid Hilger. A fast and effective determination of the biodistribution and subcellular localization of fluorescent immunoliposomes in freshly excised animal organs. *BMC biotechnology*, 17:1–11, 2017.

[58] Takuma Tsuchida, Youngmin A Lee, Naoto Fujiwara, Maria Ybanez, Brittany Allen, Sebastiao Martins, M Isabel Fiel, Nicolas Goossens, Hsin-I Chou, Yujin Hoshida, et al. A simple diet-and chemical-induced murine nash model with rapid progression of steatohepatitis, fibrosis and liver cancer. *Journal of hepatology*, 69(2):385–395, 2018.

[59] Daphne van der Heide, Ralf Weiskirchen, and Ruchi Bansal. Therapeutic targeting of hepatic macrophages for the treatment of liver diseases. *Frontiers in immunology*, 10:2852, 2019.

[60] A. van Kampen. Metabolic reprogramming of macrophages to reduce inflammation in non-alcoholic fatty liver disease (nafld). Msc thesis, University of Twente, 2023.

[61] Lian Wang, Dongguang Wang, Tianli Zhang, Yao Ma, Xiang Tong, and Hong Fan. The role of immunometabolism in macrophage polarization and its impact on acute lung injury/acute respiratory distress syndrome. *Frontiers in immunology*, 14:1117548, 2023.

[62] Yankai Wen, Joeri Lambrecht, Cynthia Ju, and Frank Tacke. Hepatic macrophages in liver homeostasis and diseases-diversity, plasticity and therapeutic opportunities. *Cellular & molecular immunology*, 18(1):45–56, 2021.

[63] Eduard Wisse, RB De Zanger, K Charels, Patrick Van Der Smissen, and RS McCuskey. The liver sieve: considerations concerning the structure and function of endothelial fenestrae, the sinusoidal wall and the space of disse. *Hepatology*, 5(4):683–692, 1985.

[64] Jing Zeng, Jian-Gao Fan, and Sven M Francque. Therapeutic management of metabolic dysfunction associated steatotic liver disease. *United European Gastroenterology Journal*, 12(2):177–186, 2024.